Surface Modification of Rutile TiO_2 with Alkaline Earth Oxide Nanoclusters for Enhanced Oxygen Evolution

S. Rhatigan[1], E. Sokalu[2], M. Nolan[1]✉, G. Colón[2]✉

[1]*Tyndall National Institute. University College Cork. Lee Maltings, Dyke Parade. Cork T12 R5CP. Ireland*

[2]*Instituto de Ciencia de Materiales de Sevilla. Centro Mixto Universidad de Sevilla-CSIC. Américo Vespucio s/n. 41092 Sevilla. Spain*

Abstract.

The oxygen evolution reaction (OER) is accepted as the bottleneck in overall water splitting and has seen intense interest. In this work, we have prepared rutile TiO_2 modified with nanoclusters of alkaline earth metal oxides for the OER. Photocatalytic O_2 evolution reaction was performed over TiO_2 rutile surface-modified with alkaline earth oxide nanoclusters, namely CaO and MgO. The O_2 evolution activity is notably enhanced for MgO modified systems at low loadings and a combination of characterisation and first principles simulations allows the interpretation of the role of the nanocluster modification on improving photocatalytic performance of alkaline earth modified rutile TiO_2. At such low loadings, the nanocluster modifiers would be small and this facilitates close correlation with theoretical models. The structural and surface characterisation of the modified systems indicate that the integrity of the rutile phase is maintained after modification. However, charge carrier separation is strongly affected by the presence of surface nanoclusters. This improved performance is related to surface features such as higher ion dispersion and surface

✉ Corresponding authors: michael.nolan@tyndall.ie and gcolon@icmse.csic.es

hydroxylation, which are also discussed with first principles simulations. The modified systems are reducible so that Ti^{3+} ions will be present. Water dissociation is favourable at cluster and interfacial sites of the stoichiometric and reduced modified surfaces. Pathways to water oxidation at interfacial sites of reduced MgO-modified rutile TiO_2 are identified, requiring overpotentials of 0.68 V. In contrast, CaO-modified systems required overpotentials in excess of 0.85 V for the reaction to proceed.

Keywords: TiO_2; surface modification; alkaline earth oxide nanocluster; photocatalysis; O_2 evolution.

1. Introduction.

Since the discovery of photocatalytic water cleavage, significant effort has been put into developing new photocatalyst materials for water splitting, and some excellent results have been obtained.[1-5] Nevertheless, the efficiencies achieved are still far from those required for practical applications. The overall water splitting reaction consists of two half reactions, the hydrogen evolution reaction (HER) and oxygen evolution reaction (OER). While H_2 production from aqueous solutions containing sacrificial reagents has been demonstrated to be quite an efficient process, the OER remains a challenging redox process and is the limiting reaction in overall water splitting. Hence, the development of a highly active photocatalyst for the OER is important for enhancing the efficiency of solar-driven hydrogen production technologies.

Titania surfaces, modified with dispersed nanoclusters of other materials, have been studied for a variety of photocatalytic applications.[6-22] This strategy differs from doping schemes as the modification is at the titania surface rather than through incorporation of other species into the titania lattice. The key feature of surface modified systems is the interface between the support and the nanocluster modifier, similar to work on supported metal catalysts. The visible light response of the catalyst can be enhanced through a dual consequence of favourable alignment of band energies and new active sites that arise from the modification with the nanoclusters. The usual benchmark material, TiO_2 P25, consists of interfaced rutile and anatase phases and shows enhanced photocatalytic activity, which is proposed to arise from suitable band alignments and enhanced electron and hole separation upon light absorption.[23, 24] Heterostructures of different metal oxides sharing an interface have also shown enhanced photocatalytic performance.[21, 25-28]

Moreover, nanostructured metal oxides are considered promising photocatalysts due to enhanced surface area and the presence of low-coordinated metal and oxygen sites for the adsorption of feedstock species.[29-32] Thus, the surface modification of titania with nanoclusters of other materials can combine the favourable features of heterostructuring and nanostructures. This approach has also been shown to suppress electron-hole recombination *via* the promotion of charge carrier separation.[7, 12, 14] In addition, first principles studies show surface-modified titania systems to be more reducible, with oxygen vacancies forming spontaneously or with a significant reduction in the formation energies compared to unmodified TiO_2.[6, 8, 12] This is an important aspect of this surface modification approach as oxygen vacancies are active sites in

metal oxide catalysts[33-35] and reduced Ti^{3+} cations play a crucial role in the chemistry at titania surfaces.[36, 37]

Catalysts based on metal oxides are widely used[38-40] for the OER and first principles studies have examined reaction pathways for water oxidation at oxide surfaces.[41-44] In general, these studies focus on the free energies of four proton-coupled electron transfer (PCET) steps involved in the following reaction:

$$2H_2O \rightarrow O_2 + 4(H^+ + e^-) \quad (1)$$

By examining the relative stability of the surface-bound intermediates, it is possible to identify the reaction step that requires the highest free energy input and hence compute the overpotential required to render each step thermodynamically favourable. The overpotential, η_{OER}, is determined from:

$$\eta_{OER} = \frac{\max[\Delta G_{OER}]}{e} - 1.23\,V$$

where $\max[\Delta G_{OER}]$ is the highest free energy step in eV, e is the electron charge and 1.23 V is the theoretical potential for O-H cleavage. Further details on this model, and its application in the current work, will be discussed in the following sections and the *Supporting Information (SI)*.

A DFT study of water oxidation at rutile-type oxides computed overpotentials of 0.37, 0.56 and 1.19 V at the (110) surfaces of RuO_2, IrO_2 and TiO_2, respectively.[45] The overpotential required for rutile TiO_2 was revised to 0.97 V in a subsequent paper by the same authors.[41] Another first principles study of water oxidation at CeO_2 nanorods attributed an important role to oxygen vacancies in improving the production of O intermediates.[46] Ulman *et al* reported overpotentials of ~0.8 V for water oxidation at hematite surfaces with various terminations.[47] Moreover, upon modification of the hematite surface with Ga_2O_3, the overpotential was computed as ~0.95 V. Consistent across the surfaces studied by Ulman *et al* is the overpotential-determining step, which involves dehydrogenation of surface-bound hydroxyls.

In this work, we present an experimental and theoretical study of rutile TiO_2 modified with nanoclusters of the alkaline earth oxides (AEO) CaO and MgO and their application in the oxygen evolution reaction. The combination of experiment and computation yields a comprehensive and cohesive analysis of the activity of the novel AEO-modified rutile TiO_2 catalyst for the OER.

The preparation method in this work, incipient impregnation, is a well-established technique for the deposition of modifiers at semiconductor surfaces.[48-50] A similar synthesis approach has been used to deposit nanoclusters of PtO_x,[48, 51] SnO_x,[51] ZnO,[52] and MoO_3,[53] on TiO_2. Thus, based on this synthesis procedure, the rutile TiO_2 surface will be modified with dispersed AEO nanoclusters, rather than being doped with the alkaline earths incorporated onto lattice sites. Samples were prepared with different loadings of the AEO nanocluster modifiers and the performance of nanocluster modified TiO_2 as a catalyst for the OER was determined.

In our DFT calculations, we implement the standard model approach [REFERENCES]which has been widely reported in the literature; the outputs of this model are generally accepted as material descriptors for the photocatalytic performance. We apply this model approach to provide a comprehensive analysis of the OER activity of the new AEO-modified TiO_2 catalysts and this is complemented by direct comparisons with experiment.

Alkaline earth oxide modification has been previously reported to enhance the photoactivity of anatase TiO_2 for dye degradation or H_2 production using Pt as a co-catalyst.[54, 55] However, as far as we know, this is the first time that the use of alkaline earth oxide nanocluster modification of rutile for OER is reported. **Scheme 1** summarises the experimental and modelling approach in developing alkaline earth oxide nanocluster modified rutile for OER.

Scheme 1: Multistep preparation synthetic route for alkaline earth oxide supported on rutile TiO_2. Rational design and photocatalytic studies for OER.

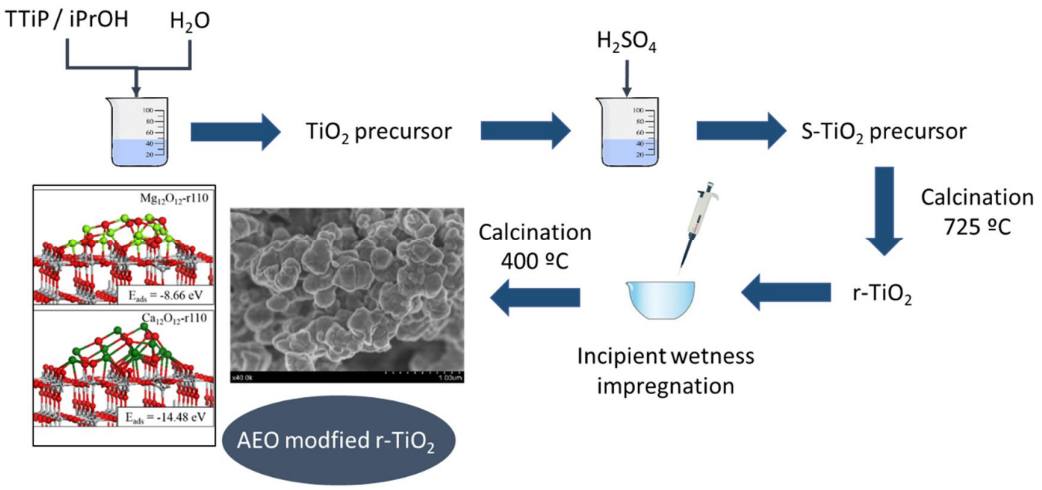

We observe clear differences in the activities of CaO- and MgO-modified TiO_2 for OER, depending on the loading of the AEO nanocluster. In particular, low coverages of highly-dispersed MgO-nanoclusters yield a significant enhancement, doubling the photonic efficiency relative to unmodified rutile.

To investigate this result further, we characterise the modified surfaces experimentally and computationally. The structure of the heterostructured surfaces was investigated *via* X-ray diffraction (XRD) and X-ray photoelectron spectroscopy (XPS). Further insight into this characterisation is provided though DFT calculations. We examine the aggregation of the nanoclusters at the rutile surface and, by comparison with metal-oxygen binding energies and formation energies, explain trends in the dispersion of the nanoclusters at the rutile surface. In addition, we assess the reducibility, *via* oxygen vacancy formation, of the composite systems.

UV-vis diffuse reflectance spectroscopy and photoluminescence (PL) spectroscopy are used to assess the impact of modification on the light absorption properties and charge carrier dynamics, respectively. The analysis is supported by DFT computations of the density of states (DOS) and a model for photoexcitation, through which we assess the stability of the excited state and the localisation of photogenerated electrons and holes.

To investigate active sites of AEO-modified TiO_2 for the OER, we use DFT calculations to examine water adsorption at various sites of the stoichiometric and reduced nanocluster modified surfaces. This includes water adsorption at nanocluster sites, adsorption at the interface between the nanocluster modifier and the titania surface, and water adsorption at an already hydroxylated heterostructure. Here, we note that many DFT studies of water oxidation at surfaces ignore the role of surface hydroxylation. We find that reduction of the system, and the presence of reduced Ti^{3+} cations, play a crucial role in the photocatalytic performance by stabilising OER intermediates at the surface. Moreover, we identify interfacial sites as active sites and this, importantly, indicates that small, dispersed nanoclusters will yield the highest OER activity.

2. Methodology

2.1 Catalyst preparation

The TiO_2 system was prepared by a sol-gel method using titanium tetraisopropoxide (TTIP) as precursor (20 mL TTIP) in isopropanol (40 mL iPrOH). Forced hydrolysis of the TTIP solution was achieved by adding a certain volume of bidistilled water (20 mL). The white precipitate was then filtered and washed several times with water and methanol. Finally, the resulting solid was dried overnight at 90 ºC. Amorphous TiO_2 was submitted to a sulfation step prior to calcination. Thus, TiO_2 precursor was immersed in 1 M sulphuric acid solution for 1 hour upon stirring. This pre-treatment will hinder the anatase to rutile phase transition to high temperature.[56] The suspension was then filtered again, the precipitate dried at 90 ºC overnight and calcined at 725 ºC for 2 hours, after which we obtain TiO_2 showing mainly rutile structure.

M-TiO_2 (M = Mg^{2+} and Ca^{2+}) systems were obtained by incipient impregnation of the corresponding nitrate precursor with a loading range between 0.05 at% to 3 at%. The obtained impregnated powder was dried at 90 ºC and then calcined at 400 ºC for 1 hour for the elimination of nitrates.

Details of the methods of characterisation of the modified systems are provided in the *SI*.

2.2 Photocatalytic runs

Photocatalytic O_2 production tests were performed in a flow-reactor system (**Figure S1**). The powder photocatalysts were suspended in $AgNO_3$ water solution (0.02 M) that acts as an electron trapping sacrificial agent. The reaction media was continuously thermostated at 20ºC ± 1ºC to prevent any temperature effect. The catalyst suspension (0.5 g/L) was firstly degassed with an N_2 stream (100 mL/min) for 15 min. After that, the N_2 flow was settled at 15 mL/min and stabilised for 30 min. This nitrogen flow was used to displace the oxygen produced from the photoreactor headspace towards the GC measuring system. Then, the lamp (125 W medium pressure Hg lamp) was switched on and the effluent gases were analysed to quantify O_2 production by gas chromatography (Agilent 490 micro GC) using a thermal conductivity detector.

The photonic efficiency for the O_2 evolution reaction has been determined from the reaction rate and the flux of incoming photons (calculated for the irradiation wavelengths of 365 nm).[57]

2.3 DFT calculations

The spin-polarised DFT calculations were performed with the VASP5.4[58, 59] code using projector augmented wave (PAW) potentials[60, 61] and the Perdew-Wang (PW91)[62] approximation to the exchange correlation functional. The plane-wave energy cut-off was 400 eV; Ti is described with 12 valence electrons, Mg and Ca with 8, O with 6 and H with 1. The convergence criteria for the energy and forces were 10^{-4} eV and 0.02 eV $Å^{-2}$, respectively. The k-points were sampled at the Γ-point and aspherical gradient corrections were applied throughout. Gaussian smearing with $\sigma = 0.1$ eV was implemented in calculations of the density of states (DOS). This set-up is consistent with our previous work on similar systems, which facilitates comparison.

A Hubbard U correction was applied to the Ti *3d* states with U(Ti) = 4.5 eV, consistent with previous work.[63-68] This correction is necessary in describing the partially filled *d*-orbital and reduced Ti^{3+} states.[69, 70] An additional +U correction was applied to the O *2p* states (U(O) = 5.5 eV) in the photo-excited state model to describe hole localisation. The +U correction for O *2p* states is necessary to obtain a localised O polaron[6, 8, 12] and this is only required in the photoexcitation model; implementing +U on O *2p* states for other calculations would make comparisons with computational studies in the literature difficult. The goal of this model is to obtain a qualitative description of the localisation and stability of photoexcited charges; comparing the results between the bare surface and after AEO-modification shows the impact of modification on charge carrier separation.

Further details regarding construction of the models and their computational characterisation is provided in the *SI*.

3. Results and Discussion

3.1 *Photocatalytic performance for water oxidation*

A series of MgO- and CaO-nanocluster modified rutile samples were prepared with alkaline earth loadings ranging from 0.05-3 at.%, using the impregnation procedure outlined in the experimental section (see *SI)*. In **Figure 1** we show the photoactivity of the alkaline-earth modified rutile materials for the OER, with a silver nitrate electron scavenger. The photoactivity of bare TiO_2 for OER is notable compared with other reports in the literature.[71-73] Such outstanding photoactivity could be associated with the structural and surface feature

as we will describe later. In fact, pre-sulfation treatment has demonstrated to improve significantly the photocatalytic performance of anatase TiO_2 for phenol degradation reaction.[74] Depending on the loading of the modifier, surface modification of rutile with both nanocluster of MgO and CaO can lead to improvements in the OER activity and the photonic efficiency.

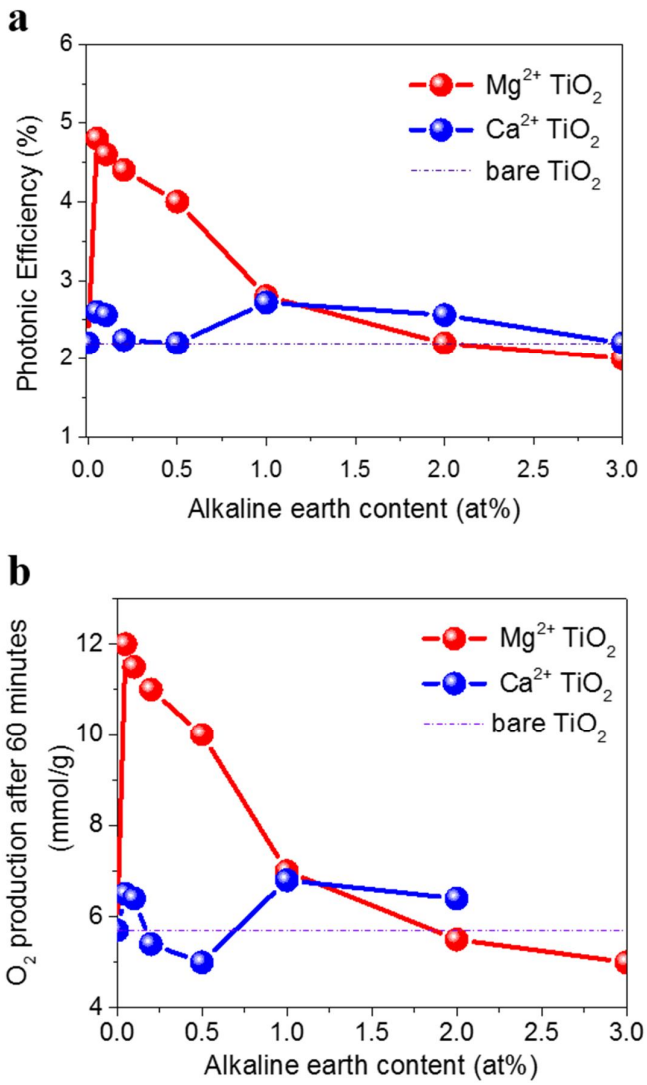

Figure 1. (a) Photonic efficiencies for MgO- and CaO-modified TiO_2 for the OER. (b) Photocatalytic O_2 evolution (mmol/g) after 60 min for MgO- and CaO-modified TiO_2 (0.5 g/L catalyst, 0.02 M $AgNO_3$, Hg lamp 125 W).

This improvement is particularly notable for MgO-modified TiO_2 (**Figure 1**). In particular, for an MgO loading of 0.05 at.%, the achieved photonic efficiency and the O_2 production after 60 minutes are double that measured for bare TiO_2 rutile. This is a remarkable result considering the extremely low level of surface modification. The efficiency decays as the Mg^{2+} content increases, eventually reaching photoactivities similar to those of bare TiO_2 for loadings of 2-3

at.%. Such an effect has been observed in other studies of surface-modification schemes, where increased loadings of the modifier have a detrimental effect on the activity.[71, 75, 76] This suggests a bi-functionality, where sites of both the surface and the modifier play a role in the catalytic activity and a key role for nanostructured MgO supported on TiO_2.

As mentioned before, the comparison of the OER efficiency with other reported systems is quite complex since the reaction operational parameters are different and the photonic efficiencies are not provided. In any case, the optimum O_2 yield obtained in the present work is notable with respect to similar systems.

Table 1. Surface features of AEO-modified rutile TiO_2 from XPS.

AE-modified TiO_2		**Binding Energy (eV)**			**AE/Ti ratio**	**O/Ti**	**OH (%)**
		Mg 1*s*	**Ca 2*p***	**Ti *2p***			
Bare TiO_2		---	---	458.7	---	2.21	11.0
Mg^{2+}	0.10	1303.9	---	458.7	0.015	2.54	36.1
	1.00	1303.7	---	458.4	0.587	2.88	27.0
	2.00	1303.8	---	458.3	0.796	2.90	19.5
	3.00	1303.6	---	458.2	0.867	2.64	18.0
Ca^{2+}	0.10	---	347.2	458.3	0.107	2.32	9.2
	1.00	---	347.1	458.3	0.147	2.87	16.9
	2.00	---	347.4	458.2	0.260	2.79	14.0
	3.00	---	346.5	458.2	0.479	3.08	21.9

For CaO modification, the highest efficiency is attained at a higher Ca^{2+} ion content compared to Mg^{2+} but the improvement is less significant compared to MgO modification. It is clear that the presence of these modifiers affects the photocatalytic activity of rutile TiO_2 in different ways. To understand the influence of AEO-modification we have performed a wide surface, structural and electronic characterisation of the catalysts. This analysis is complemented by

first principles calculations, with particular focus on identifying active sites of water oxidation at the AEO-modified TiO_2 surface.

3.2 Structural and Surface Characterisation of AEO-nanocluster modified Rutile TiO_2

We have prepared TiO_2 rutile by precipitation and further sulphuric acid pre-treatment. As previously reported sulphuric acid pre-treatment prior to the calcination step delays the anatase to rutile transformation and favours the formation of a well-crystallised anatase structure with relatively high surface area.[74] Thus, the presence of surface anchored sulfate groups stabilises the anatase structure at high temperatures, such as 650ºC. The transition to rutile phase takes place once surface sulfates evolve during calcination. By calcination at 725 ºC, the obtained TiO_2 materials show a dominant rutile phase with a crystallite size of 55 nm, which denotes a high degree of crystallisation (**Figure 2.a**).

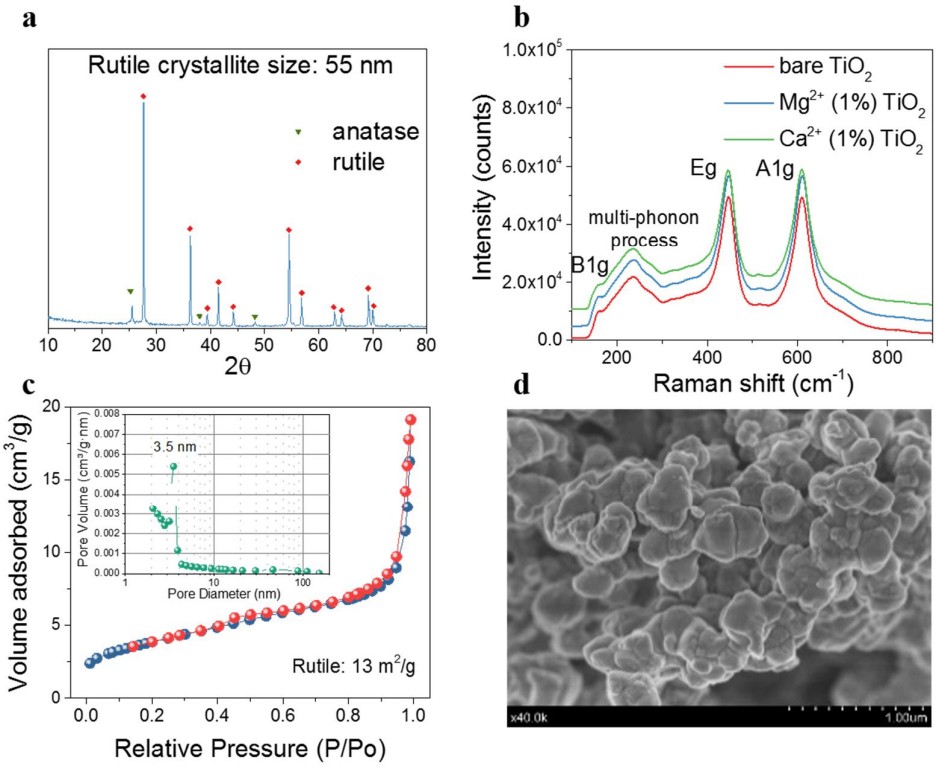

Figure 2. Structural and textural properties of TiO_2 rutile photocatalysts: a) XRD pattern of r-TiO_2 support; b) Raman spectra of bare r-TiO_2 and alkaline modified r-TiO_2; c) N_2 adsorption-desorption isotherm (inset: pore size distribution plot) of r-TiO_2 support; d) SEM image of r-TiO_2 support.

Raman spectra in **Figure 2.b** provide further evidence of the predominance of the rutile phase. Thus, characteristic rutile Raman modes at 157 cm^{-1} (B1g), 235 cm^{-1} (multi-phonon process), 447 cm^{-1} (Eg) and 610 cm^{-1} (A1g) are present. Since Raman spectroscopy is very sensitive to different crystalline structures, in accordance with the XRD data, tiny bands corresponding to the anatase phase can be seen. There are no strong distortions or shifts of the Raman modes after modification with the alkaline earths, indicating that there is no doping of the metals onto Ti sites in the rutile lattice. Doping would result in formation of oxygen vacancies to compensate the lower oxidation state of Mg and Ca, which would distort the local atomic structure and hence the Raman peaks. Due to the high calcination temperature to assure the rutile phase, the TiO_2 support shows a notably low specific surface area of 13 m^2/g, with a negligible porosity (**Figure 2.c**). As expected, the impregnation with the alkaline-earth oxide nanoclusters does not induce any notable change in the structure of modified rutile. The morphology of the sample in **Figure 2.d** for TiO_2 rutile from SEM also confirms the sample sintering due to the high calcination temperature (**Figure 2.d**).

The presence and dispersion of alkaline-earth ions at the rutile surface have been studied by XPS analysis. In **Figure 3** we show the Mg *1s* and Ca *2p* XPS spectra for samples with different coverages of the alkaline earth. The core electron binding energy is 1304 eV for Mg *1s* and 347 eV for Ca *2p*, which correspond in both cases to Mg^{2+} and Ca^{2+} (**Table 1**).[77, 78] For Ti *2p*, the observed binding energies all lie around 458.5 eV, which is the typical value for Ti^{4+} in TiO_2. With the introduction of the alkaline earth modifiers, there is a small shift in the Ti *2p* position towards lower binding energies. This shift has also been observed for Mg modified systems and indicates the formation of Ti-O-Mg bonds,[79] which would be present with alkaline earth oxide nanoclusters supported on the rutile TiO_2 surface coordinating to surface oxygen atoms.

By considering the chemical features of the surface, it is possible to see an important difference between Mg and Ca modification. Firstly, considering the atomic ratio of the alkaline earth to Ti^{4+} from XPS and presented in **Table 1**, the Mg/Ti ratio for MgO-modified TiO_2 at the lowest loadings is significantly lower when compared to the Ca-modification at the same nominal loading and compared to higher Mg-loadings. This suggests a higher dispersion of Mg^{2+} at the rutile surface, but this dispersion is not observed for Ca^{2+}, even at the lowest loadings. Moreover, as the alkaline-earth content increases, the AE/Ti ratio progressively increases for both modifiers, which denotes a lower degree of dispersion. This can be due to the formation of larger sized nanoclusters due to aggregation at the surface. For higher content samples, Ca/Ti atomic ratios are significantly lower than for Mg.

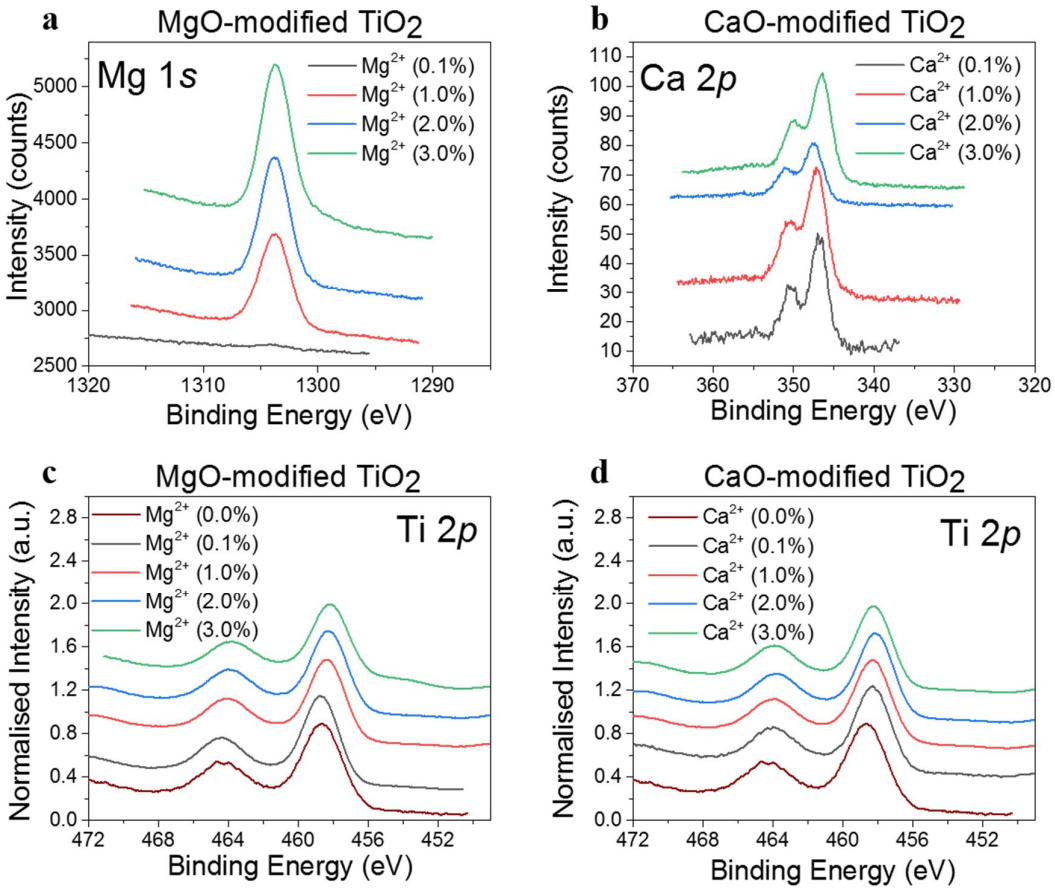

Figure 3. XPS spectra for alkaline earth modified TiO_2 rutile photocatalysts.

With regard to the degree of hydroxylation of the modified samples, the MgO-modified TiO_2 samples with the lowest loadings show the highest level of surface hydroxylation, 36.1% for 0.1% Mg, and we note that the trends in hydroxylation coverage with the loading of the alkaline earth behave differently for MgO and CaO. For MgO modified rutile, the higher dispersion of Mg^{2+} ions at low coverages appears to favour hydroxylation. For example, the sample with Mg 0.1 at.% shows both high dispersion (lower Mg/Ti value of 0.015) and a high degree of surface hydroxylation (36.1%). This effect is not observed for the CaO-modified series, for which the hydroxylation coverage increases as the Ca^{2+} content increases.

This result is consistent with previous work which showed that water dissociation is favourable for MgO nanoclusters supported on TiO_2[7] and on ultra-thin MgO films supported on metals (Ag and Mo), but is not favourable on bulk MgO or beyond 3 monolayer (ML) thick films.[80-

[82] Therefore as the loading of Mg increases, hydroxylation will become less favourable. By contrast, previous work clearly shows that water dissociation is favourable on CaO films and on the (100) bulk cleaved surface[83, 84] so that the degree of hydroxylation, as a result of water dissociation at the oxide, increases with an increase in the loading of CaO on rutile.

Further insight into the dispersion of AEO nanoclusters at the titania surface is provided by DFT calculations. To model AEO-modified rutile TiO_2, the most stable rutile facet, the (110) surface, is modified with MgO and CaO nanoclusters of three compositions, 4-, 8-, and 12-MgO/CaO units, denoted M_4O_4-, M_8O_8-, and $M_{12}O_{12}$-r110 (M = Mg, Ca). The starting geometries for these clusters were published in the work of Haertelt *et al.*[85] In this way, we investigate the effects of dispersion/aggregation and coverage for comparison with experimental results. The stable, relaxed geometries and computed adsorption energies for the 4-, 8-, and 12-unit clusters of MgO and CaO adsorbed at the rutile (110) surface are shown in **Figure 4**. Additional geometries and discussion are presented in the *SI* (**Figures S4** and **S5**).

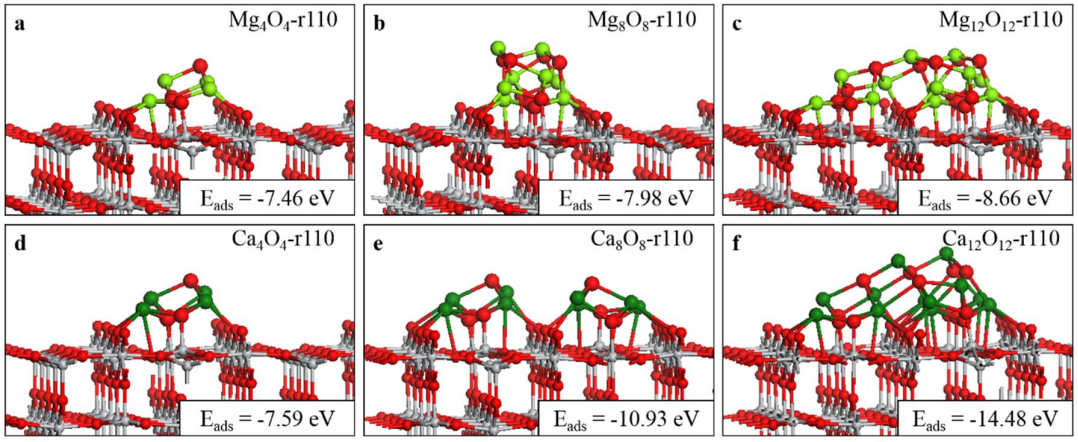

Figure 4. The top panels show the relaxed atomic structure of rutile (110) modified with nanoclusters of composition (a) Mg_4O_4, (b) Mg_8O_8 and (c) $Mg_{12}O_{12}$. The bottom panels show the relaxed atomic structure of rutile (110) modified with nanoclusters of composition (d) Ca_4O_4, (e) Ca_8O_8 and (f) $Ca_{12}O_{12}$. The adsorption energies are included in the insets. In this and subsequent figures Ti is represented by grey spheres, O by red, Mg by light green and Ca by dark green. Atoms of the nanoclusters have been enlarged.

These modified surfaces do not necessarily represent global minima, as the space of possible adsorption configurations is too large to easily investigate. Rather, the geometries shown in **Figure 4** are representative structures for which we may compute material descriptors relevant

to the photocatalytic activity. They are the most favourable structures we have found in our search of different configurations. Previous work on modified metal oxide surfaces shows that key properties determining the chemistry of these structures are not sensitive to the precise adsorption structure of the modifiers at the surface. The properties of the modified surface are consistent, so long as the nanocluster modifier binds with the surface through new interfacial bonds; that is, new bonds that form between cations and anions in the surface and the nanocluster.[86] To explore this, we analysed in detail a less stable $Mg_{12}O_{12}$-r110 geometry, **Figure S4.a**, for which the results are discussed in the *SI*. This analysis shows that there are small quantitative, but not qualitative, differences in the computed properties so that the sensitivity to the precise structure is not significant.

In each structure shown in **Figure 4**, the adsorbed geometry of the nanocluster differs considerably from the most stable gas-phase structures. These are taken from ref.[85] and our relaxed structures are shown in **Figure S2**. Upon relaxation, it is more energetically favourable for the MgO and CaO nanoclusters to wet over the rutile surface. This is driven by the formation of interfacial bonds between surface Ti and nanocluster oxygen as well as surface oxygen and nanocluster cations. These bonds anchor the nanoclusters at the rutile surface. For the example of Mg_4O_4-r110, (**Figure 4.a**), 8 interfacial bonds are established between the cluster and the surface. Of these 3 are Ti to nanocluster oxygen (O_C) bonds, 4 are Mg to bridging surface oxygen (O_{br}) bonds and there is a single Mg to surface in-plane oxygen (O_{ip}) bond.

For the Mg_8O_8 and $Mg_{12}O_{12}$ nanocluster, we can adsorb a single nanocluster or two/three Mg_4O_4 nanoclusters. The most stable relaxed geometries result from an initial structure whereby the nanoclusters are adsorbed as two and three Mg_4O_4 units, shown in **Figures 4.b** and **4.c**. In the relaxed heterostructures the surface Ti to O_C distances are 1.76-2.12 Å. Distances for Mg to surface oxygen sites are 1.92-2.45 Å for O_{br} and 2.10-2.38 Å for O_{ip}.

The CaO-TiO_2 surface modification shows similar changes in the nanocluster structures upon adsorption and relaxation. The relaxed Ca_4O_4-r110 structure (**Figure 4.d**) is qualitatively similar to that of Mg_4O_4-r110 (**Figure 4.a**), with the formation of 8 interfacial bonds, consisting of 3 Ti-O_C bonds, 4 Ca-O_{br} bonds and 1 Ca-O_{ip} bond. For Ca_8O_8-r110 (**Figure 4.e**), the most stable adsorption configuration is that in which two Ca_4O_4 nanoclusters are adsorbed in proximity but without interacting *via* shared bonds. The most stable $Ca_{12}O_{12}$-r110 structure (**Figure 4.f**) corresponds to three Ca_4O_4 nanoclusters in a contiguous cluster at the surface. The Ti-O_C bond lengths from the surface to the nanocluster are 1.80-1.94 Å, the Ca-O_{br} and Ca-O_{ip}

bond lengths between the nanocluster and the surface are 2.14-2.93 Å and 2.43-3.05 Å, respectively.

The effect of the modification with MgO and CaO on the rutile (110) surface is most notable for those Ti ions that bind to oxygen atoms of the adsorbed nanoclusters. These Ti ions migrate out from the surface, towards the nanoclusters, by up to 0.8 Å, breaking bonds to subsurface oxygen ions. However, modification of the rutile surface with AEO-modifiers does not lead to a substantial reconstruction of the surface; this confirms the results of the experimental characterisation of the AEO-modified TiO_2 systems.

The magnitudes of the computed adsorption energies, shown in **Figure 4**, indicate that the nanoclusters adsorb strongly at rutile (110) and require significant temperatures to desorb. Mg_4O_4 and Ca_4O_4 have similar computed adsorption energies, -7.46 eV and -7.59 eV, while differences emerge in the computed adsorption energies of the larger nanoclusters. The adsorption energies for Mg_8O_8 and $Mg_{12}O_{12}$ are -7.98 eV and -8.66 eV, respectively, which are comparable to that of Mg_4O_4, indicating that there is little energy gained in the aggregation of MgO to form larger nanoclusters at the surface. Conversely, Ca_8O_8 and $Ca_{12}O_{12}$ have computed adsorption energies of -10.93 eV and -14.48 eV, which, although not so large as to prohibit the dispersion of smaller clusters at the surface, indicate that aggregation to larger clusters is preferred for CaO. These results are consistent with the experimental analysis that for low Mg contents, the MgO modifier is highly dispersed at the rutile surface whereas CaO will be less dispersed and present as larger structures.

As the loading increases, the configurations in which the modifiers form contiguous clusters, as shown in **Figures 4.c** and **4.f**, are more stable by similar amounts, 2.25 eV for $Mg_{12}O_{12}$ and 2.11 eV for $Ca_{12}O_{12}$, than the next most stable configurations, which consist of three isolated Mg_4O_4 and Ca_4O_4 nanoclusters, shown in **Figures S4** and **S5** of the *SI*.

To investigate these trends in aggregation, we compare the per-unit binding energies of the AEO nanoclusters, as shown in the *SI*. The binding energies of the 4-, 8-, and 12-unit MgO nanoclusters are -2.93, -3.76 and -4.14 eV, respectively; for CaO, the binding energies are -4.16, -4.56, and -4.86 eV. A similar trend was reported by Malliavin *et al* in their study of $(MgO)_n$ and $(CaO)_n$ clusters with $n \leq 6$.[87] Similarly, bulk calculations for the formation energies of Mg-O and Ca-O showed that CaO has a larger formation energy (-6.55 eV) compared to MgO (-6.12 eV).[88] Moreover, Chen and colleagues reported greater stability of MgO nanoclusters relative to bulk MgO, as compared with the stability of CaO nanoclusters

relative to CaO bulk.[89, 90] These results suggest that CaO favours aggregation to larger structures compared to MgO. Moreover, for the 12-unit nanoclusters at the rutile surface, there are 23 interfacial Ca-O bonds formed, compared with 13 interfacial Mg-O bonds; this is likely the result of the larger ionic radius of Ca^{2+} (1.06 Å) compared to Mg^{2+} (0.78 Å)[90] and indicates a stronger interaction of CaO at the rutile surface.

To examine reducibility, the formation of a neutral oxygen vacancy was investigated at each oxygen site in the supported nanoclusters. The most stable structures with one oxygen vacancy are shown in **Figure 5**, along with the computed formation energies. The full set of oxygen vacancy formation energies is included in **Table S4** the *SI*. On all MgO-modified and CaO-modified TiO_2 structures the energy cost to produce an oxygen vacancy increases with the size of the nanocluster. This is in agreement with an increase in the M-O binding energy with increasing nanocluster size.[87] Despite this, the modified surfaces are clearly more reducible than bare rutile (110), for which the computed energy cost to produce a single oxygen vacancy from a bridging oxygen site is +4.50 eV.

On MgO-modified rutile TiO_2, the formation energies in **Figures 5.a**, **5.b** and **5.c** suggest that reducibility is enhanced at the lowest loadings, in which small MgO clusters are widely dispersed over the surface. As the coverage increases, and the modifiers aggregate to form larger nanoclusters, the energy cost to produce an oxygen vacancy increases. Similarly, for CaO modifiers, oxygen vacancy formation is computed to have lower energy costs for smaller clusters. However, for CaO-modified TiO_2, aggregation to form larger clusters is favourable, even at lower coverages and this, combined with larger binding energies for CaO nanoclusters, means that the formation energies for oxygen vacancies are larger than on MgO-TiO_2.

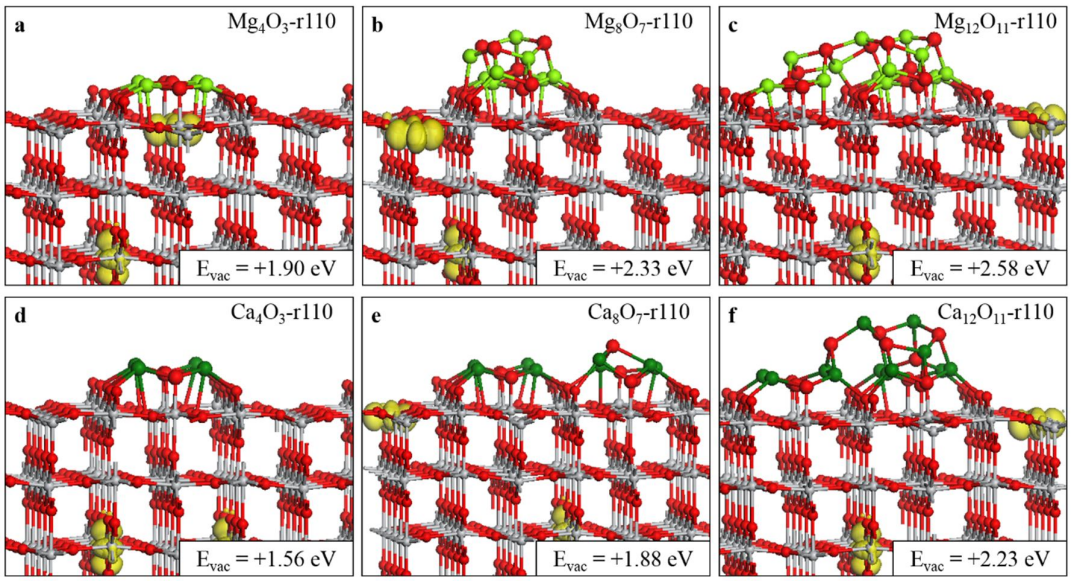

Figure 5. Relaxed atomic structures of AEO-modified rutile (110) with a single, reducing oxygen vacancy. Top panels show (a) Mg_4O_3-, (b) Mg_8O_7- and (c) $Mg_{12}O_{11}$-r110. Bottom panels show (d) Ca_4O_3-, (e) Ca_8O_7- and (f) $Ca_{12}O_{11}$-r110. The yellow isosurfaces enclose spin densities of up to 0.02 eV/Å^3.

After formation of a neutral oxygen vacancy, two electrons are released and their localisation is visualised with the excess spin density plots in **Figure 5**. These charge distributions emerge after relaxation of the systems with one O ion removed. In all cases, the two electrons localise on Ti sites on the rutile (110) surface, since Mg is not reducible. One electron localises at a subsurface Ti site, typical for reduced rutile (110).[91, 92] While there are studies in the literature showing that there are different energetics of different Ti^{3+} localisation patterns in unmodified rutile (110),[91, 92] we stress that in our nanocluster-modified rutile structures, structural distortions are already present in the surface layer of the rutile substrate, which will promote the localisation of the second electron.

While the impact of electron localisation on different Ti sites could be examined, this will not change the key finding that the cost to remove an oxygen is significantly lower in surface modified rutile compared to the bare surface. The location of the second electron depends on the size of the modifier. On all reduced MgO-r110 structures, the second electron localises at a surface Ti. For Ca_4O_3-r110, both electrons localise at sub-surface Ti sites, while Ca_8O_7-r110 and $Ca_{12}O_{11}$-r110 show electron localisation similar to the corresponding MgO-TiO_2 structures. The electron localisation at Ti sites is further confirmed by an increase in the

computed Bader charge of Ti from 9.6-9.7 electrons, for Ti^{4+}, to 9.9-10.0 electrons, for Ti^{3+},[6, 7, 12] while the computed spin magnetisations for Ti^{3+} sites are in the range 0.8-0.9 μ_B. Finally, the Ti^{3+}-O distances increase by up to 0.2 Å.

3.3 Effect of AEO Nanoclusters Modification on Light absorption

The UV-vis diffuse reflectance spectrum is presented in **Figure 6.a**. Unmodified rutile and MgO- and CaO-modified rutile show similar band gaps around 3.1 eV, typical for the TiO_2 rutile phase.[93] However, if we examine closely the absorption edge, it is clear that for the MgO and CaO modified samples, some light absorption is apparent in the visible range. This absorption should correspond to the emergence of states in the TiO_2 valance to conduction band energy gap, due to the presence of the modifier or vacancies at the rutile surface. This red-shift in absorption is more pronounced for Ca^{2+} modified TiO_2.

DFT insights into the optical properties of AEO-modified TiO_2 rutile are provided through analysis of the computed projected electronic density of states (PEDOS), focused on the 4- and 12-unit nanoclusters modifying the TiO_2 surface. **Figure 6** displays the PEDOS plots for the stoichiometric ground states (**Figure 6.b**, **6.c**) and the reduced states, in which one oxygen vacancy is present, as described in Section 2.2, (**Figure 6.d**, **6.e)**. The top half of each panel shows the contribution to the PEDOS from Ti-3*d* and Mg/Ca-(*s* + *p*) states while the bottom half shows the 2*p* states of surface oxygen (O_S) and nanocluster oxygen (O_C). The PEDOS for the bare rutile (110) surface is given in **Figure S7** in the *SI* for comparison and within our computational set-up the valence to conduction band energy gap is 2.2 eV. This underestimation of the energy gap is of course typical of approximate DFT methods and while it is possible to tune the +U correction to reproduce the experimental band-gap, this results in a poorer description of other material properties and so is not advised. Rather, the Coulomb correction is implemented to overcome the self-interaction error (SIE) of standard DFT and to describe localised electronic states. However, comparison of the PEDOS across the different modified TiO_2 structures yields qualitative information about the impact of AEO-modification.

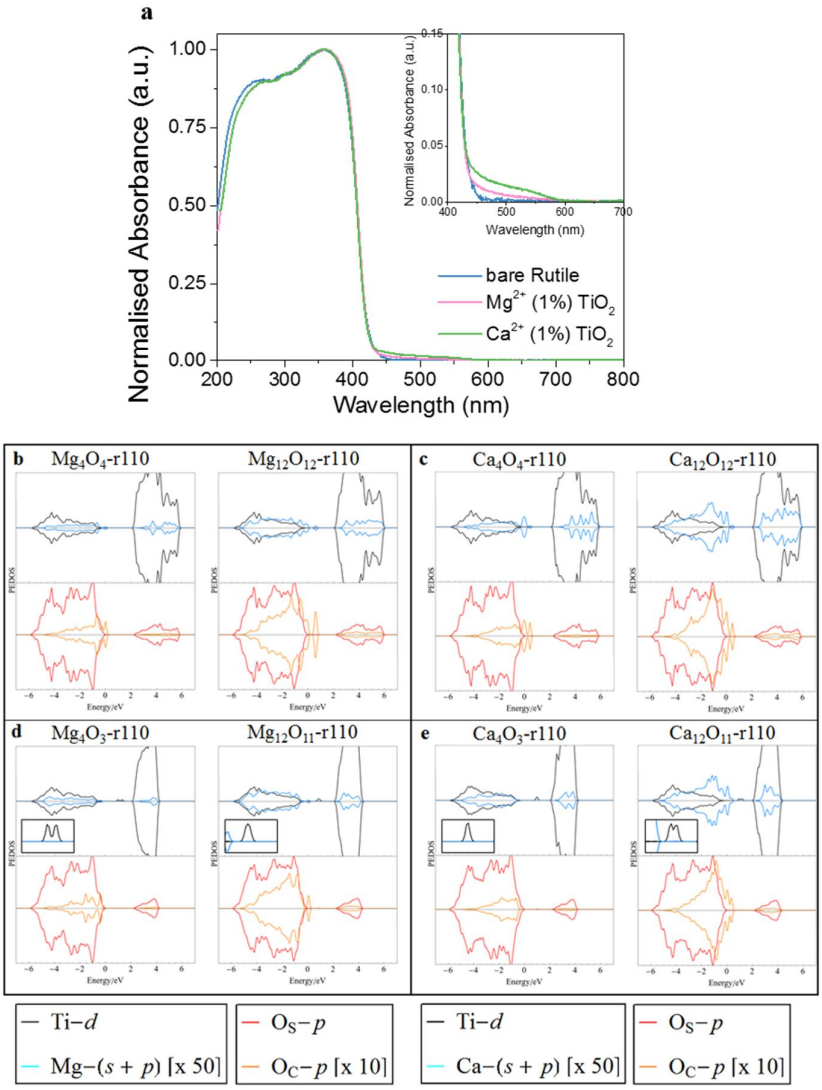

Figure 6. Optical properties of AEO-modified TiO_2 rutile photocatalysts. (a) Absorption spectra for MgO- and CaO-modified rutile TiO_2 (1 at.%). (b)-(e) Computed projected electronic density of states (PEDOS) plots for AEO-modified rutile (110). Top panels display the PEDOS for the stoichiometric ground states (b) Mg_4O_4-r110 and $Mg_{12}O_{12}$-r110 and (c) Ca_4O_4-r110 and $Ca_{12}O_{12}$-r110. The PEDOS in the bottom panels were computed after formation of a single oxygen vacancy and represent (d) Mg_4O_3-r110 and $Mg_{12}O_{11}$-r110 and (e) Ca_4O_3-r110 and $Ca_{12}O_{11}$-r110. The top half of each plot shows the contributions due to Ti-*d* (black) and M-(*s* + *p*) (M = Mg, Ca; blue). The bottom half of each plot displays O_S-*p* (red) and O_C-*p* (orange) contributions. The rutile (110) VBM is set to 0 eV and the insets in the bottom panels show occupied Ti^{3+} states in the band-gap in the range [0 eV, 2 eV].

For stoichiometric structures, the computed PEDOS predicts a small red-shift in the band gap due to modifier-derived O 2*p*-states extending the valence band maximum (VBM) to higher energy and this effect is greater for the larger modifiers, and for CaO when compared to MgO. After modification, Ti 3*d*-states continue to dominate the conduction band minimum (CBM)

with unoccupied Mg- and Ca-derived states lying higher in energy. For the reduced structures, the smaller nanoclusters show no O_C-derived states above the VBM of the TiO_2 support. Mid-gap states, due to reduced Ti^{3+}, emerge at 1.0 eV and 1.3 eV above the VBM for Mg_4O_3-r110 (the two peaks result from an asymmetric distribution of the two electrons) and at 1.0 eV above the VBM for Ca_4O_3-r110. Similarly, for $Mg_{12}O_{11}$-r110, high lying O_C states are removed so that fewer nanocluster-derived states are present above the titania VBM and Ti^{3+} states emerge in the band gap at 0.9 eV. For $Ca_{12}O_{11}$-r110, cluster-derived states persist above the VBM after oxygen vacancy formation and Ti^{3+} states emerge at 1.0 eV and 1.2 eV above the VBM.

In the context of measurements of the absorption edge of MgO-modified rutile TiO_2, at 1 at.% loading, analysis of the computed PEDOS for such a system, namely Mg_4O_3-r110 (**Figure 6.d**), suggests that any impact on the light absorption properties will be minimal and due only to transitions from occupied Ti^{3+} states which emerge in the band-gap after reduction. For CaO-modification, the computed PEDOS plots indicate a potential red-shift in the absorption edge due to cluster-derived states above the titania VBM. While oxygen vacancy formation is promoted in CaO-r110 relative to unmodified rutile, the effect on the valence band edge persists after reduction in the case of larger CaO nanoclusters.

3.4 Photoluminesence and Charge Separation

The influence of alkaline-earth modification on the charge carrier dynamics can be assessed using photoluminescence spectroscopy (**Figure 7.a**). In both cases, the presence of MgO and CaO induces a reduction in the magnitude of the PL signal compared to unmodified rutile TiO_2, upon excitation at 320 nm. Therefore, it can be inferred that the surface modification with these alkaline-earth ions enhances the separation of photogenerated charges and suppresses electron-hole recombination. Similar behaviour was reported by other authors for alkaline-earth doped ZnO systems.[77] In that case, the difference in PL signal observed for doped systems was associated to the different ionic radii. In our case, small interesting differences can be noticed between Mg^{2+} and Ca^{2+}. While for Mg^{2+} the PL signal is not strongly affected by the loading, for Ca^{2+} the modification with 0.05 at.% shows somewhat higher PL when compared to higher Ca^{2+} content.

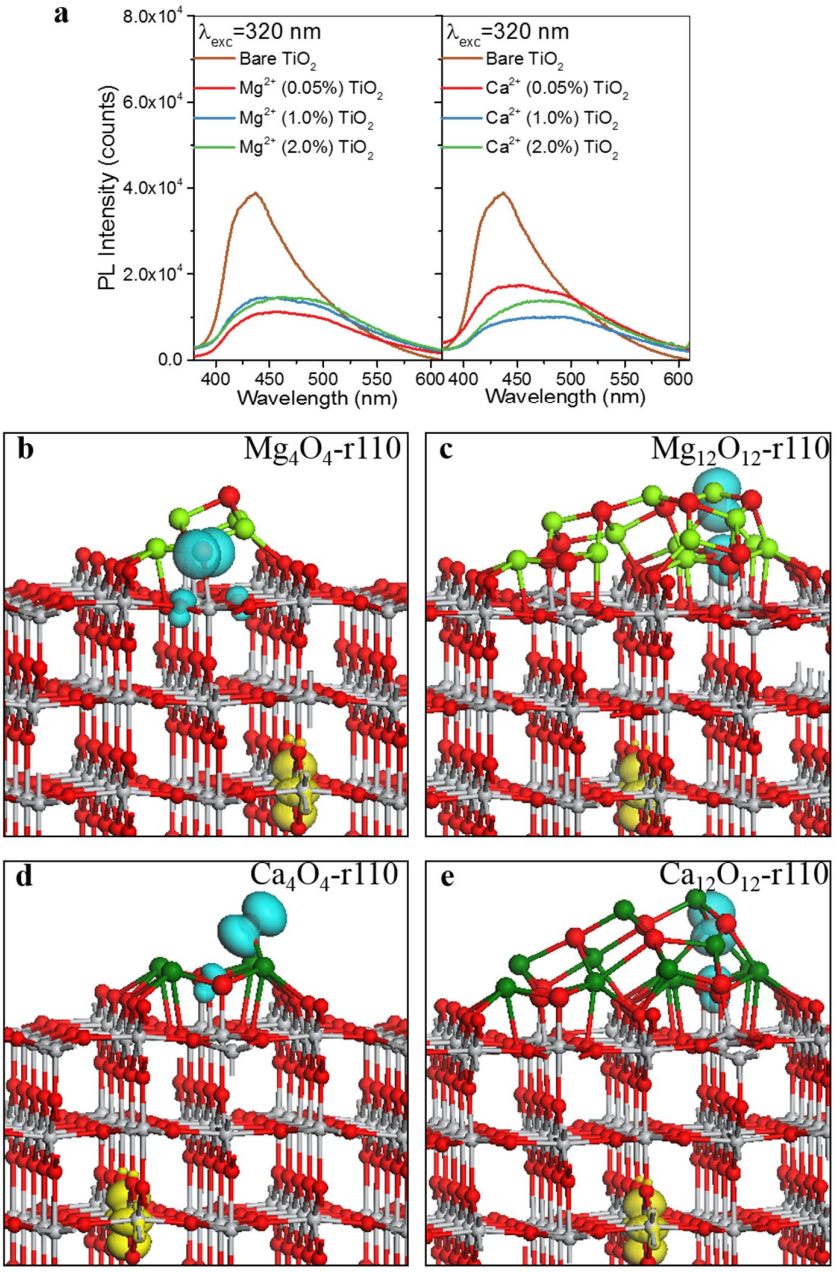

Figure 7. (a) Photoluminescence spectra for Mg^{2+} and Ca^{2+} modified TiO_2 upon excitation at 320 nm. Spin density plots for the photoexcited model applied to (b) Mg_4O_4-r110, (c) $Mg_{12}O_{12}$-r110, (d) Ca_4O_4-r110 and (e) $Ca_{12}O_{12}$-110. Localisation of electron and holes is indicated by yellow and blue isosurfaces, respectively, which enclose spin densities up to 0.02 eV/Å^3.

Thus, both MgO and CaO positively influence the charge separation upon excitation. In addition, for CaO modified systems we have observed a slight absorption in the visible range, probably due to intermediate states in the bandgap. However, the better photocatalytic behaviour shown by MgO modified TiO_2 is likely correlated with the surface features of the heterostructure, as already discussed, i.e. MgO modified TiO_2 at low loadings exhibits a high degree of surface hydroxylation, as well as a notable Mg^{2+} ion dispersion, compared to the CaO modified systems. In addition, the supported MgO nanoclusters are more reducible than the supported CaO-nanoclusters.

To explore the impact of AEO-modification on charge carrier separation and localisation within DFT, we impose a triplet electronic state and compute the vertical and singlet-triplet as well as the electron-hole relaxation (trapping) energies (see *SI* and ref. [6, 8, 12] for full details). These energies are presented in **Table S5** and values computed for the bare rutile (110) surface are included for reference. The values for $E^{vertical}$ represent the simple VB-CB energy difference and are analogous to the optical band gap. Hence, the energy gap for bare rutile (110) is 2.35 eV, and again, the underestimation of the bandgap, which is inherent in approximate DFT, persists with our computational set-up. However, the photoexcitation model provides qualitative information about the effect of surface modification on the light absorption properties, charge localisation and the stability of photoexcited charges.

The results in **Table S5** show that modification of rutile (110) with the smaller nanoclusters, Mg_4O_4 and Ca_4O_4, has little effect on the optical band-gap; values for $E^{vertical}$ of 2.28 eV and 2.39 eV are computed for the surfaces modified with these nanoclusters. Surface modification with the larger nanoclusters, $Mg_{12}O_{12}$ and $Ca_{12}O_{12}$, yields values for $E^{vertical}$ of 1.98 eV and 2.06 eV, corresponding to decreases of 0.4 eV and 0.3 eV, respectively, so that at higher coverages, a small red shift in light absorption is predicted.

The values for E^{excite}, which is the energy difference between the fully relaxed triplet state and singlet ground state, accounts for structural relaxations and polaron formation in response to electron and hole localisation in the triplet electronic state. The energy gain in relaxation in the excited state is given by the values for E^{relax}, which represent the stability of the photogenerated electron-hole pairs and their trapping. The values for E^{relax} are considerably larger for the modified surfaces (1.06-2.20 eV) relative to that computed for the bare rutile (110) surface, 0.50 eV. This reflects the greater degree of structural relaxation that is possible in nanocluster-

modified TiO_2 to accommodate the polarons formed in the triplet electronic state and suggests the photoexcited electron and hole will be more stable in the modified rutile structures.

Another important factor in the stability of photoexcited charges is their spatial separation, which we assess through analysis of the excess spin density and the computed Bader charges. The excess spin density plots are shown in **Figure 7**. The charge localisation scheme is similar for each AEO-modified TiO_2 structure. The photoexcited holes localise at oxygen sites on the nanocluster and the electrons localise at subsurface Ti sites in rutile (110). For Mg_4O_4-r110, an originally three-fold coordinated O_C ion is now two-fold coordinated after hole localisation. For $Mg_{12}O_{12}$-r110, the O_C ion at which the hole state localises is three-fold coordinated to Mg ions both before and after photoexcitation; however, the Mg-O_C bond lengths increase by as much as 0.3 Å in the excited state.

For Ca_4O_4-r110, the O_C ion at which the hole localises is two-fold coordinated to Ca ions and was originally three-fold coordinated in the ground state. For $Ca_{12}O_{12}$-r110, after hole localisation at O_C, the ion remains three-fold coordinated, however, the Ca-O_C bond lengths increase by 0.2 Å.

Hole localisation at O_C ions is confirmed by a change in the computed Bader charge from 7.2 to 6.8 electrons and a computed spin magnetisation of 0.7 μ_B. These values are typical of oxygen hole polaron formation. For those Ti sites at which the photoexcited electrons localise, the Bader charges increase from 9.6 to 9.9 electrons and the computed spin magnetisations are 0.8 μ_B, indicating reduction to Ti^{3+}. The results of this model suggest that modification of rutile (110) with AEO nanoclusters can promote the separation of photoexcited electrons and holes and thereby suppress charge carrier recombination, corroborating analysis of the PL spectra.

4. Origin of Enhanced Oxygen Evolution on *AEO* Nanoclusters Modified Rutile (110)

4.1 Water Adsorption at AEO Nanoclusters Modified Rutile (110)

To better understand the improved OER activity on MgO-modified TiO_2, we studied water adsorption at MgO- and CaO-modified rutile (110) and the subsequent water oxidation pathways with the standard DFT model approach for OER.[41-44] We investigated multiple

adsorption configurations of water at each stoichiometric and reduced AEO-modified rutile surface. Three adsorption schemes were considered:

- adsorption of water at sites on the nanocluster,
- adsorption of water at an interfacial site between the modifier and the rutile surface,
- adsorption of a second water at the interface site with dissociatively adsorbed water already present on the nanocluster.

The last model aims to elucidate the impact of hydroxylation, which has been shown to be important on AEO-modified TiO_2 structures, on the relative stabilities of the water oxidation intermediates and the free energies of each step in the OER model.

Table S6 presents the computed adsorption energies of water at different sites at AEO-modified TiO_2. The adsorption geometries are shown in **Figures S8-S13** in the *SI*. For all adsorption sites, the adsorption of one water molecule is exothermic and leads to spontaneous dissociation to produce surface-bound hydroxyls. In the stoichiometric systems, the computed dissociative adsorption energies of water, at sites of the nanoclusters, are between -2.3 eV and -3.5 eV, which provides an origin for the previously discussed hydroxylation of the AEO-modified materials. The computed adsorption energies for water at the same cluster sites on reduced AEO-TiO_2 are in the range of -2.4 eV to -1.5 eV, somewhat moderated from the stoichiometric cluster, but still highly exothermic. Thus, the nanocluster modifiers will promote hydroxyl formation through water dissociation. The atomic structure of these adsorption sites is shown in **Figures S8** and **S9**.

For the interfacial adsorption sites, shown in **Figures S10** and **S11** for the stoichiometric and reduced surfaces, respectively, the computed adsorption energies are less obviously dependent on whether the surface is stoichiometric or reduced. In addition, these are clearly less exothermic than adsorption on the nanocluster, with computed adsorption energies in the range of -1.2 eV to -1.0 eV. The exception is for water adsorbed at the interfacial site of $Ca_{12}O_{12}$-r110 for which the computed adsorption energy is -1.6 eV (**Figure S10**).

After the dissociative adsorption of the first water molecule at cluster sites, the computed adsorption energies for the subsequent adsorption of a second water at interfacial sites of the modified surfaces are in the range of -1.6 eV to -0.9 eV. These results indicate that, for the coverages investigated, hydroxylation of the modifiers has little impact on water adsorption at interfacial sites. The adsorption geometries for water adsorbed at interfacial sites of AEO-

modified surfaces, in which the modifiers are hydroxylated, are shown in **Figure S12** and **S13** for the stoichiometric and reduced systems, respectively.

In the following, we analyse the OER using a widely accepted[41-44] model for the water oxidation pathway. This pathway consists of four PCET steps, where (*) represents the AEO-rutile structure::

(A) $H_2O + (*) \rightarrow {}^*OH + (H^+ + e^-)$

(B) ${}^*OH \rightarrow {}^*O + (H^+ + e^-)$

(C) $H_2O + {}^*O \rightarrow {}^*OOH + (H^+ + e^-)$

(D) ${}^*OOH \rightarrow O_2 + (*) + (H^+ + e^-)$

The free energy of reaction "X" is calculated as:

$$\Delta G_X = \Delta E_X + \Delta ZPE - T\Delta S \quad (4)$$

In the above, ΔE_X is the difference in total energy, computed *via* DFT, between the products and reactants. The difference in zero-point energies, ΔZPE, is derived from vibrational frequencies computed with DFT and the entropic contribution, $T\Delta S$, is taken from tabulated values for the gas phase molecules and neglected for adsorbed species

Steps A and C each describe water adsorption events, however, water dissociation upon adsorption and the first dehydrogenation are dealt with implicitly as a single step. For an explicit description, we may consider these steps as consisting of sub-steps, which for water adsorption in dissociated form, may be expressed as follows, where (*) represents the AEO-rutile structure:

(A1) $H_2O + (*) \rightarrow {}^*OH + {}^*H$

(A2) ${}^*OH + {}^*H \rightarrow {}^*OH + (H^+ + e^-)$

And

(C1) $H_2O + {}^*O \rightarrow {}^*OOH + {}^*H$

(C2) ${}^*OOH + {}^*H \rightarrow {}^*OOH + (H^+ + e^-)$

The overall free energy of a given step is then the sum of the free energies of the sub-steps, so that: $\Delta G_X = \Delta G_{X1} + \Delta G_{X2}$. The *SI* provides a detailed discussion of the set-up for the water oxidation analysis.

In general, we find that for water adsorbed at stoichiometric AEO-TiO_2, the surface-bound intermediates of the water oxidation pathway have high free energy costs for the subsequent

OER steps. This is due to localisation of hole states at surface-bound *O species after dehydrogenation (sub-step A2 and step B) of the hydroxyls produced from dissociative water adsorption.

This effect is mitigated for the reduced systems because electrons can transfer from a reduced Ti^{3+} site to stabilise under-coordinated *O species. Spin magnetisations of 0.4-1.0 μ_B were computed for *O species after dehydrogenation at the stoichiometric systems. At reduced AEO-TiO_2, the same *O species have spin magnetisations of 0 μ_B indicating a charge transfer from TiO_2 to *O. At the same time, Ti ions of the surface cycle between Ti^{3+} and Ti^{4+}, indicated by computed spin magnetisations of 0.8-0.9 μ_B and 0 μ_B, before and after formation of *O, respectively. After each dehydrogenation, one Ti^{3+} is oxidised to Ti^{4+}, with the electron transferring to the resulting *O species. Moreover, for water oxidation at cluster sites of the reduced systems, we find that the final step, evolution of a molecule of O_2, is excessively endothermic as the surface bound O_2 species is over-stabilised at cluster sites. For these reasons, we focus in particular on the OER proceeding at interfacial sites of the reduced AEO-modified surfaces.

4.2 Water oxidation at interfacial sites of AEO-TiO_2

4.2.1 Water oxidation without prior AEO nanocluster hydroxylation

We consider the water oxidation pathway, using the model for water oxidation described above. This model was applied to the bare rutile (110) surface,[41] for which the highest Gibbs free energy (ΔG) of a single step (*viz* the dehydrogenation of a surface OH group) was computed as +2.20 eV (step A). In identifying favourable reaction pathways at the modified surfaces, we consider that should the free energy cost of any PCET step (indicated previously as A, B, C or D in section 3.1) exceed 2.20 eV there will be no enhancement in the OER over bare rutile (110).

We use reduced AEO-modified rutile as a model system because the ease of reduction means that oxygen vacancies will be present and, as discussed, the OER at the stoichiometric surface is not favoured. We summarise the results of the calculations of steps A-D in the OER, without and with hydroxylation of the AEO nanocluster, in **Table 2**.

The adsorption geometries in **Figures S11** and **S13** show water molecules dissociatively adsorbed at interfacial sites of the reduced AEO-modified systems, both without and with

hydroxylation of the nanocluster. At the interfacial site, the water-derived hydroxyl group is bound to a Ti site of the surface and a second hydroxyl forms after migration of the other hydrogen from water to bind with an O_C site. Adsorption of OH at a Ti site results in the Ti ions migrating out from the surface and breaking a bond with subsurface oxygen.

Table 2. Computed free energies for water oxidation PCET steps starting from a single water molecule adsorbed at interfacial sites of AEO-modified rutile (110) in the reduced state with one oxygen vacancy.

1 x H_2O	**Mg_4O_3-r110**	**$Mg_{12}O_{11}$-r110**	**Ca_4O_3-r110**	**$Ca_{12}O_{11}$-r110**
	ΔG (eV)	**ΔG (eV)**	**ΔG (eV)**	**ΔG (eV)**
Step A1	-0.53	-0.50	-0.34	-0.32
Step A2	0.81	0.52	0.62	0.64
Step A	**0.28**	**0.02**	**0.29**	**0.32**
Step B	**0.82**	**1.84**	**0.99**	**1.03**
Step C1	1.49	0.01	-0.96	2.61
Step C2	0.31	1.95	2.25	0.38
Step C	**1.79**	**1.96**	**1.29**	**2.99**
Step D	**2.03**	**1.09**	**2.35**	**0.58**
Sum	**4.92**	**4.92**	**4.92**	**4.92**

The adsorption geometries that are shown in **Figure S11** represent the end of sub-step A1, *viz* dissociative water adsorption at the interface of the reduced AEO nanocluster and the rutile support. The computed free energies of this and subsequent steps are presented in **Table 2**. Only two of the reaction pathways shown in **Table 2** meet the criterion that each PCET step has a computed ΔG of less than +2.20 eV. These are both for water oxidation on the reduced MgO-TiO_2 structures.

On all reduced AEO-modified TiO_2 structures, sub-step A1 is exothermic, with computed ΔG_{A1} in the range -0.53 eV to -0.32 eV. The first dehydrogenation step (sub-step A2) is moderately uphill, with ΔG_{A2} in the range +0.56 eV to +0.85 eV. Thus, the PCET step A proceeds with overall free energies in the range +0.02 eV to +0.32 eV.

The second dehydrogenation (step B) requires a larger free energy cost, with computed ΔG_B in the range +0.82 eV to +1.84 eV. These free energies are however, well below the value of

+2.20 eV, computed for bare rutile. After step B, a terminal oxygen ion is singly coordinated to a Ti ion of the surface and acts as a site for the adsorption of a second water molecule for step C.

The computed free energies of step C are in the range +1.29 to +1.96 eV, with the exception of $Ca_{12}O_{11}$-r110 for which ΔG_C is +2.99 eV, which is significantly larger than the same energy step for bare rutile. Step D involves the evolution of O_2 accompanied by the release of the fourth proton and an electron. For Mg_4O_3-r110 and $Mg_{12}O_{11}$-r110 the computed free energies are +2.03 eV and +1.09 eV, respectively. For Ca_4O_3-r110, the computed free energy, ΔG_D, is +2.35 eV and so this pathway requires a larger energy input than that computed for bare rutile (110).

The intermediate states of the water oxidation pathway proceeding at the interfacial site of reduced $Mg_{12}O_{11}$-r110 (with no nanocluster hydroxylation) are shown in **Figure 8**, and for Mg_4O_3-r110 in **Figure S14**. The first dehydrogenation, step A, is most favourable from the surface-bound hydroxyl group and leaves a terminal *O species and a hydroxyl group on the cluster. Step B involves dehydrogenation of the cluster-bound hydroxyl so that the reduced $Mg_{12}O_{11}$ nanocluster and the terminal *O species remain at the rutile (110) surface.

After the second water adsorption (sub-step C1), *O and *OH species are bound to the surface Ti site and a second hydroxyl forms due to migration of the H atom to oxygen on the nanocluster. In sub-step C2, dehydrogenation occurs from the *OH species bound at the Ti site so that after relaxation, two *O species are bound to the same Ti site of the surface. In step D, these *O species desorb, as does the cluster-bound H atom.

The energy profiles in **Figures 8** and **S14** are based on the free energies presented in **Table 2** with the inclusion of a potential bias term, ΔG_U, which shifts the free energy of each PCET step by an amount $-eU$, where U is the electrode potential relative to the standard hydrogen electrode. For each profile we consider three applied biases: $U = 0\,V$; the equilibrium potential: $U = 1.23\,V$; and the potential at which each PCET step becomes downhill in free energy. The difference between this potential and 1.23 V is the overpotential required for the oxygen evolution reaction to proceed at the modified TiO_2 surface.

From the free energy profile, we see that at the equilibrium potential, 1.23 V, steps B and C are uphill and an applied bias of 1.96 V is required to render all steps downhill, corresponding to an overpotential of 0.73 V. Similarly, for the Mg_4O_3-r110 surface, as discussed in the *SI*, the computed overpotential is 0.80 V. For Ca_4O_3-r110 and $Ca_{12}O_{11}$-r110, the computed

overpotentials are 1.07 V and 1.76 V respectively. This means that water oxidation is inhibited compared to the bare rutile surface. This result is reflected in the experimental findings of decreased oxygen evolution activity for CaO-modified rutile at low loadings.

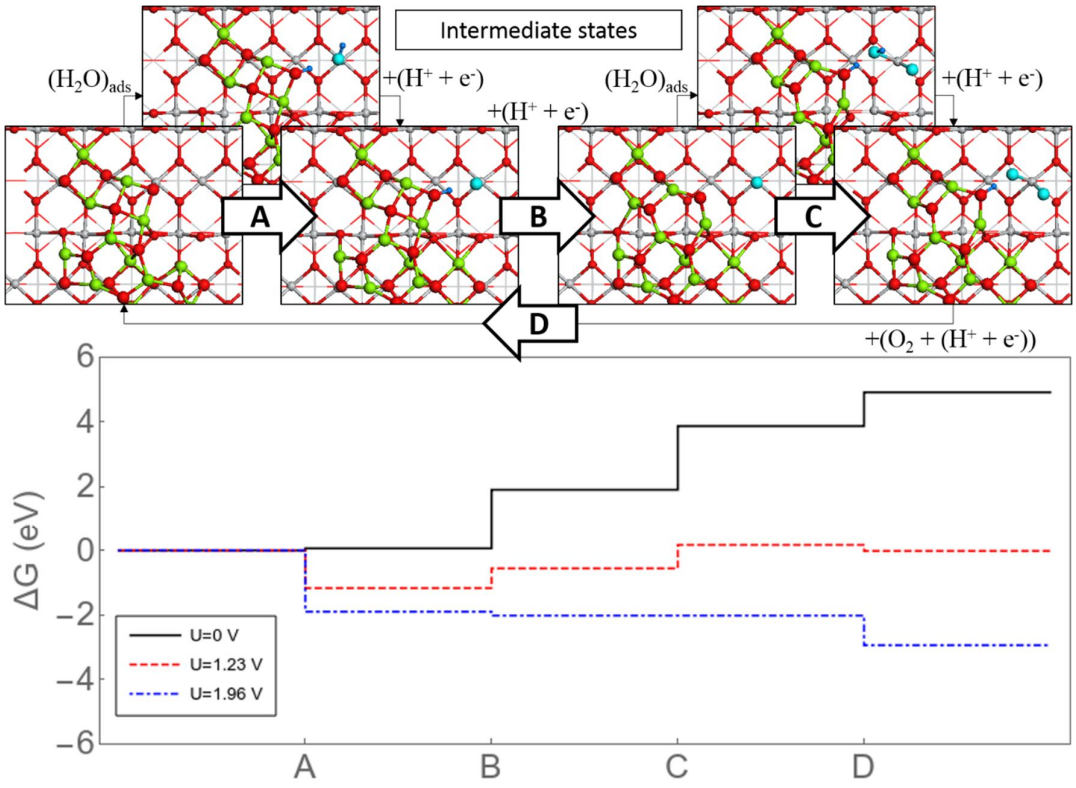

Figure 8 Reaction pathway for water oxidation starting from dissociative water adsorption at an interfacial site of the reduced $Mg_{12}O_{11}$-r110 composite surface. The free energy profile of the pathway is shown for overpotentials U = 0, 1.23 and 1.96 V. At the equilibrium potential, U = 1.23 V, steps C and D are uphill and at U = 1.96 eV all reaction steps are downhill in free energy. The intermediate states in the upper panels represent the end-points of reaction sub-steps A1 and C1. In this figure, water-derived O ions are light blue and H ions are dark blue.

These results compare with an overpotential of 0.97 V, computed for water oxidation at the bare rutile surface by Valdés *et al*[41] and indicates a favourable effect of the MgO-modifier. On hematite, the highest free energy cost is 1.82 eV, which corresponds to an overpotential of 0.71 V, given that the authors computed a free energy of 1.11 eV per PCET step.[42] A more recent study of OER at hematite surfaces demonstrated a considerable reduction in the overpotential (0.47 V) after formation of oxygen vacancies in the (110) surface.[94] Similarly, oxygen vacancies reduced the overpotential by 0.3 V for water oxidation at the hematite (0001) surface.[95] A first principles study of water oxidation on pristine and oxygen-deficient barium

titanate found that, contrary to our results and experiment, the overpotential increased from 0.45 V for the pristine surface to 1.47 V in the presence of oxygen vacancies.[43] This was attributed to the strong stabilisation of *OH and *O species for the latter system, which is not observed in the current study.

4.2.2 Water oxidation with prior AEO nanocluster hydroxylation

The role of prior hydroxylation of the catalyst surface is often overlooked in first principles OER studies. In the following, we examine the impact of hydroxylation of the AEO modifiers on the water oxidation pathways. In **Table S7**, we present the computed free energies for water oxidation proceeding at interfacial sites of the reduced AEO-modified systems, in which the nanocluster is hydroxylated by dissociative water adsorption (see **Figure S13**).

For each surface, sub-step A1 is exothermic with free energies in the range -0.87 eV to -0.23 eV and the dehydrogenation step, sub-step A2, proceeds with ΔG_{A1} in the range +0.40 eV to +1.05 eV. Thus, the overall step A, has free energies between -0.03 and 0.33 eV. The dehydrogenation in step B has ΔG_B in the range +0.98 eV to +1.03 eV. These energies are comparable to those computed for the water oxidation pathway with no hydroxyls at the cluster sites; one exception is step B at $Mg_{12}O_{11}$-r110, which decreases by 0.86 eV in the presence of cluster-bound hydroxyls.

Steps C and D have the highest free energy costs, with the free energies for step C in the range +1.85 eV to +2.08 eV and free energies of +1.50 eV to +1.96 eV for step D. For Ca_4O_3-r110, step C has the highest energy cost, with ΔG_C = +2.46 eV, indicating no enhancement relative to the bare surface. This is consistent with the low OER activity measured for low Ca loadings.

However, water oxidation at the interface of $Ca_{12}O_{11}$-r110 is more favourable after hydroxylation of the cluster; the highest energy step decreases from +2.99 eV to +2.08 eV, corresponding to an overpotential of 0.85 V. Conversely, hydroxylation of the cluster in Ca_4O_3-r110 renders water oxidation less favourable and increases the required overpotential by 0.1 V.

The water oxidation pathway proceeding at the interfacial site of reduced, hydroxylated $Mg_{12}O_{11}$-r110 (Mg_4O_3-r110) is shown in **Figure S15** (**Figure S16**). The reaction site is highlighted with a black circle in the panel on the left. After water adsorption at the interfacial site, the water-derived hydroxyl is singly coordinated to a 5-fold coordinated Ti site, as previously described. The second H ion migrates to a neighbouring O_C ion.

Here we describe the reaction intermediates for $Mg_{12}O_{11}$-r110 and the details for Mg_4O_3-r110 are provided in the *SI*. The first dehydrogenation is most favourable from the cluster-bound hydroxyl group and leaves a *OH species bound at the rutile (110) surface. After step B the terminal *O species remains at the surface. After the water adsorption described by sub-step C1, an *OOH species is bound to the surface Ti site and a second hydroxyl forms due to migration of the H atom to an O_C site. In sub-step C2, dehydrogenation occurs from the *OOH species bound at the Ti site so that after relaxation, an $*O_2$ species is bound to the surface. In step D, the O_2 molecule evolves with the release of the cluster-bound H atom.

The energy profiles in **Figures S15** and **S16** are based on the free energies presented in **Table S7**. An applied bias of 1.91 V is required to render all steps downhill, corresponding to an overpotential of 0.68 V. Similarly, for the Mg_4O_3-r110 surface, as discussed in the *SI*, the computed overpotential is 0.74 V.

In summary, we identify water oxidation proceeding favourably at *interfacial sites* of reduced MgO-modified rutile (110), with lower free energy costs for the PCET steps compared to water oxidation at rutile (110). These results highlight the role played by oxygen vacancies and the presence of reduced cations (Ti^{3+}), which are produced by enhanced reduction of the MgO-TiO_2 system, in promoting the oxygen evolution reaction. Furthermore, there is an important role of the water adsorption site, where water adsorption at the interface of the nanocluster modifier and the support is the most active site for OER. We also see that, after an initial dissociative water adsorption at cluster sites, water oxidation proceeds with similar energy costs at interfacial sites of Mg_4O_3-r110 and $Mg_{12}O_{11}$-r110; the values for ΔG are within 0.1 eV for these surfaces, with and without cluster-bound hydroxyls.

While quantifying these results in the context of measured oxygen evolution activities is beyond the scope of the current models, our results corroborate those of experiment. We confirm an enhancement for water oxidation at MgO-modified rutile at low loadings and a negative impact due to CaO-modification, relative to unmodified TiO_2.

5. Conclusion

By simple surface modification of TiO_2 rutile with nanoscale MgO and CaO, the photoactivity for O_2 evolution can be improved. The enhancement in O_2 evolution is considerable for MgO at very low loadings and high dispersion, and decreases at higher loadings. From this we infer

that both the surface and modifier are involved in the water oxidation reaction and this is confirmed by a first principles investigation of active sites of the nanocluster-modified surfaces. From the range of AEO modifier contents examined, it is expected that the modifier is present as a nanocluster on the rutile surface. This feature permits a close correlation with our theoretical models, and indeed, we achieved good agreement between experimental and computational results. In addition, the results show that the modifier must be in the nanocluster regime to modify the chemistry of the TiO_2 support effectively.

From the structural and textural properties, the surface modification does not induce any major changes to rutile. However, the charge carrier dynamics are improved by the presence of alkaline ions at low loadings, which leads to lower recombination. DFT simulations show that the spatial separation of electrons and holes is promoted for the modified systems. It has also been stated that alkaline ion dispersion on TiO_2 surface was better for Mg^{2+} than for Ca^{2+}. This high dispersion on Mg^{2+} at very low content is also accompanied by a higher hydroxylation degree. The greater dispersion of MgO at the surface was confirmed by first principles calculations, which indicate that aggregation of CaO to larger clusters is favoured.

Oxygen vacancies form with moderate energy costs for the modified systems, leading to the reduction of Ti^{4+} to Ti^{3+}. This has consequences for the DOS, however, the impact of modification on the light absorption properties was found to be small, both experimentally and based on computational results.

Using a model for the water oxidation pathway we have computed the applied overpotential required for the OER to proceed. In general, for water adsorbed at cluster sites, the surface bound intermediates are over-stabilised, impeding the reaction. We have identified a reaction pathway that proceeds at interfacial sites of the reduced MgO-modified systems, which drives an enhancement of the O_2 evolution activity relative to bare rutile TiO_2.

These results highlight the importance of nanocluster modifiers, oxygen vacancies and Ti reduction in promoting the OER and identifies interfacial sites present at low coverages of nanocluster MgO as active sites for water oxidation. Moreover, this model confirms the enhanced performance for MgO-modification, relative to CaO-modification. Thus, by rational design, we have interpreted and explained the better photocatalytic performance that arises from alkaline earth modification of rutile TiO_2, particularly Mg^{2+} modification at low loading.

Acknowledgements

We acknowledge the financial support by PCIN-2017-056 project from M-ERA.Net programme through VICYT. SR and MN acknowledge support from Science Foundation Ireland through the US-Ireland R&D Partnership program, Grant number SFI/US/14/E2915 and the ERA.Net for Materials Research and Innovation (M-ERA.Net 2), Horizon 2020 grant agreement number 685451, SFI Grant Number SFI/16/M-ERA/3418 (RATOCAT). We acknowledge access to SFI funded computing resources at Tyndall Institute and the SFI/HEA funded Irish Centre for High End Computing.

References

1. Kubacka, A.; Fernández-García, M.; Colón, G., Advanced Nanoarchitectures for Solar Photocatalytic Applications. *Chemical Reviews* **2012,** *112* (3), 1555-1614.
2. Colón, G., Towards the hydrogen production by photocatalysis. *Applied Catalysis A: General* **2016,** *518*, 48-59.
3. Fajrina, N.; Tahir, M., A critical review in strategies to improve photocatalytic water splitting towards hydrogen production. *International Journal of Hydrogen Energy* **2019,** *44* (2), 540-577.
4. Maeda, K.; Domen, K., Photocatalytic Water Splitting: Recent Progress and Future Challenges. *The Journal of Physical Chemistry Letters* **2010,** *1* (18), 2655-2661.
5. Wang, Z.; Li, C.; Domen, K., Recent developments in heterogeneous photocatalysts for solar-driven overall water splitting. *Chemical Society Reviews* **2019,** *48* (7), 2109-2125.
6. Rhatigan, S.; Nolan, M., Activation of Water on MnOx-Nanocluster-Modified Rutile (110) and Anatase (101) TiO2 and the Role of Cation Reduction. *Frontiers in Chemistry* **2019,** *7* (67).
7. Nolan, M., Alkaline earth metal oxide nanocluster modification of rutile TiO2 (110) promotes water activation and CO2 chemisorption. *Journal of Materials Chemistry A* **2018,** *6* (20), 9451-9466.
8. Rhatigan, S.; Nolan, M., CO2 and water activation on ceria nanocluster modified TiO2 rutile (110). *Journal of Materials Chemistry A* **2018,** *6* (19), 9139-9152.
9. Nolan, M.; Iwaszuk, A.; Lucid, A. K.; Carey, J. J.; Fronzi, M., Design of novel visible light active photocatalyst materials: surface modified TiO2. *Advanced Materials* **2016,** *28* (27), 5425-5446.
10. Lucid, A.; Iwaszuk, A.; Nolan, M., A first principles investigation of Bi2O3-modified TiO2 for visible light Activated photocatalysis: The role of TiO2 crystal form and the Bi3+ stereochemical lone pair. *Materials Science in Semiconductor Processing* **2014,** *25*, 59-67.
11. Nolan, M., First-principles prediction of new photocatalyst materials with visible-light absorption and improved charge separation: surface modification of rutile TiO2 with nanoclusters of MgO and Ga2O3. *ACS Applied Materials & Interfaces* **2012,** *4* (11), 5863-5871.
12. Rhatigan, S.; Nolan, M., Impact of surface hydroxylation in MgO-/SnO-nanocluster modified TiO2 anatase (101) composites on visible light absorption, charge separation and reducibility. *Chinese Chemical Letters* **2018,** *29* (6), 757-764.
13. Tada, H.; Jin, Q.; Iwaszuk, A.; Nolan, M., Molecular-scale transition metal oxide nanocluster surface-modified titanium dioxide as solar-activated environmental catalysts. *The Journal of Physical Chemistry C* **2014,** *118* (23), 12077-12086.
14. Jin, Q.; Fujishima, M.; Tada, H., Visible-light-active iron oxide-modified anatase titanium(iv) dioxide. *The Journal of Physical Chemistry C* **2011,** *115* (14), 6478-6483.
15. He, H.; Lin, J.; Fu, W.; Wang, X.; Wang, H.; Zeng, Q.; Gu, Q.; Li, Y.; Yan, C.; Tay, B. K.; Xue, C.; Hu, X.; Pantelides, S. T.; Zhou, W.; Liu, Z., MoS2/TiO2 Edge-On Heterostructure for Efficient Photocatalytic Hydrogen Evolution. *Advanced Energy Materials* **2016,** *6* (14), 1600464.
16. Moniz, S. J. A.; Shevlin, S. A.; An, X.; Guo, Z.-X.; Tang, J., Fe2O3–TiO2 Nanocomposites for Enhanced Charge Separation and Photocatalytic Activity. *Chemistry – A European Journal* **2014,** *20* (47), 15571-15579.
17. Park, J. B.; Graciani, J.; Evans, J.; Stacchiola, D.; Senanayake, S. D.; Barrio, L.; Liu, P.; Sanz, J. F.; Hrbek, J.; Rodriguez, J. A., Gold, copper, and platinum nanoparticles dispersed on CeO x/TiO2 (110) surfaces: high water-gas shift activity and the nature of the mixed-metal oxide at the nanometer level. *Journal of the American Chemical Society* **2009,** *132* (1), 356-363.
18. Park, J. B.; Graciani, J.; Evans, J.; Stacchiola, D.; Ma, S.; Liu, P.; Nambu, A.; Sanz, J. F.; Hrbek, J.; Rodriguez, J. A., High catalytic activity of Au/CeOx/TiO2(110) controlled by the nature of the mixed-

metal oxide at the nanometer level. *Proceedings of the National Academy of Sciences* **2009,** *106* (13), 4975-4980.
19. Johnston-Peck, A. C.; Senanayake, S. D.; Plata, J. J.; Kundu, S.; Xu, W.; Barrio, L.; Graciani, J.; Sanz, J. F.; Navarro, R. M.; Fierro, J. L. G.; Stach, E. A.; Rodriguez, J. A., Nature of the Mixed-Oxide Interface in Ceria–Titania Catalysts: Clusters, Chains, and Nanoparticles. *The Journal of Physical Chemistry C* **2013,** *117* (28), 14463-14471.
20. Libera, J. A.; Elam, J. W.; Sather, N. F.; Rajh, T.; Dimitrijevic, N. M., Iron(iii)-oxo centers on TiO2 for visible-light photocatalysis. *Chemistry of Materials* **2010,** *22* (2), 409-413.
21. Boppana, V. B. R.; Jiao, F.; Newby, D.; Laverock, J.; Smith, K. E.; Jumas, J. C.; Hutchings, G.; Lobo, R. F., Analysis of visible-light-active Sn(ii)–TiO2 photocatalysts. *Physical Chemistry Chemical Physics* **2013,** *15* (17), 6185-6189.
22. Bhachu, D. S.; Sathasivam, S.; Carmalt, C. J.; Parkin, I. P., PbO-Modified TiO2 Thin Films: A Route to Visible Light Photocatalysts. *Langmuir* **2014,** *30* (2), 624-630.
23. Scanlon, D. O.; Dunnill, C. W.; Buckeridge, J.; Shevlin, S. A.; Logsdail, A. J.; Woodley, S. M.; Catlow, C. R. A.; Powell, M. J.; Palgrave, R. G.; Parkin, I. P.; Watson, G. W.; Keal, T. W.; Sherwood, P.; Walsh, A.; Sokol, A. A., Band alignment of rutile and anatase TiO2. *Nature Materials* **2013,** *12*, 798.
24. Nolan, M.; Deskins, N. A.; Schwartzenberg, K. C.; Gray, K. A., Local Interfacial Structure Influences Charge Localization in Titania Composites: Beyond the Band Alignment Paradigm. *The Journal of Physical Chemistry C* **2016,** *120* (3), 1808-1815.
25. Chae, S. Y.; Lee, C. S.; Jung, H.; Joo, O.-S.; Min, B. K.; Kim, J. H.; Hwang, Y. J., Insight into Charge Separation in WO3/BiVO4 Heterojunction for Solar Water Splitting. *ACS Applied Materials & Interfaces* **2017,** *9* (23), 19780-19790.
26. Sotelo-Vazquez, C.; Quesada-Cabrera, R.; Ling, M.; Scanlon, D. O.; Kafizas, A.; Thakur, P. K.; Lee, T.-L.; Taylor, A.; Watson, G. W.; Palgrave, R. G.; Durrant, J. R.; Blackman, C. S.; Parkin, I. P., Evidence and Effect of Photogenerated Charge Transfer for Enhanced Photocatalysis in WO3/TiO2 Heterojunction Films: A Computational and Experimental Study. *Advanced Functional Materials* **2017,** *27* (18), 1605413.
27. Boppana, V. B. R.; Lobo, R. F., SnOx–ZnGa2O4 Photocatalysts with Enhanced Visible Light Activity. *ACS Catalysis* **2011,** *1* (8), 923-928.
28. Wang, J.; Li, H.; Meng, S.; Zhang, L.; Fu, X.; Chen, S., One-pot hydrothermal synthesis of highly efficient SnOx/Zn2SnO4 composite photocatalyst for the degradation of methyl orange and gaseous benzene. *Applied Catalysis B: Environmental* **2017,** *200*, 19-30.
29. Bhatia, S.; Verma, N., Photocatalytic activity of ZnO nanoparticles with optimization of defects. *Materials Research Bulletin* **2017,** *95*, 468-476.
30. Gordon, T. R.; Cargnello, M.; Paik, T.; Mangolini, F.; Weber, R. T.; Fornasiero, P.; Murray, C. B., Nonaqueous Synthesis of TiO2 Nanocrystals Using TiF4 to Engineer Morphology, Oxygen Vacancy Concentration, and Photocatalytic Activity. *Journal of the American Chemical Society* **2012,** *134* (15), 6751-6761.
31. Zhang, J.; Salles, I.; Pering, S.; Cameron, P. J.; Mattia, D.; Eslava, S., Nanostructured WO3 photoanodes for efficient water splitting via anodisation in citric acid. *RSC Advances* **2017,** *7* (56), 35221-35227.
32. Ong, C. B.; Ng, L. Y.; Mohammad, A. W., A review of ZnO nanoparticles as solar photocatalysts: Synthesis, mechanisms and applications. *Renewable and Sustainable Energy Reviews* **2018,** *81*, 536-551.
33. Henderson, M. A.; Epling, W. S.; Peden, C. H. F.; Perkins, C. L., Insights into Photoexcited Electron Scavenging Processes on TiO2 Obtained from Studies of the Reaction of O2 with OH Groups Adsorbed at Electronic Defects on TiO2(110). *The Journal of Physical Chemistry B* **2003,** *107* (2), 534-545.
34. Schaub, R.; Thostrup, P.; Lopez, N.; Lægsgaard, E.; Stensgaard, I.; Nørskov, J. K.; Besenbacher, F., Oxygen Vacancies as Active Sites for Water Dissociation on Rutile ${\mathrm{TiO}}_{2}(110)$. *Phys. Rev. Lett.* **2001,** *87* (26), 266104.

35. Mullins, D. R.; Albrecht, P. M.; Chen, T.-L.; Calaza, F. C.; Biegalski, M. D.; Christen, H. M.; Overbury, S. H., Water Dissociation on CeO2(100) and CeO2(111) Thin Films. *The Journal of Physical Chemistry C* **2012,** *116* (36), 19419-19428.
36. Lira, E.; Wendt, S.; Huo, P.; Hansen, J. Ø.; Streber, R.; Porsgaard, S.; Wei, Y.; Bechstein, R.; Lægsgaard, E.; Besenbacher, F., The Importance of Bulk Ti3+ Defects in the Oxygen Chemistry on Titania Surfaces. *Journal of the American Chemical Society* **2011,** *133* (17), 6529-6532.
37. Xiong, L.-B.; Li, J.-L.; Yang, B.; Yu, Y., Ti^{3+} in the Surface of Titanium Dioxide: Generation, Properties and Photocatalytic Application. *Journal of Nanomaterials* **2012,** *2012*, 13.
38. Smith, R. D. L.; Prévot, M. S.; Fagan, R. D.; Zhang, Z.; Sedach, P. A.; Siu, M. K. J.; Trudel, S.; Berlinguette, C. P., Photochemical Route for Accessing Amorphous Metal Oxide Materials for Water Oxidation Catalysis. *Science* **2013,** *340* (6128), 60-63.
39. Liu, X.; Cui, S.; Qian, M.; Sun, Z.; Du, P., In situ generated highly active copper oxide catalysts for the oxygen evolution reaction at low overpotential in alkaline solutions. *Chemical Communications* **2016,** *52* (32), 5546-5549.
40. Lu, Z.-X.; Shi, Y.; Yan, C.-F.; Guo, C.-Q.; Wang, Z.-D., Investigation on IrO2 supported on hydrogenated TiO2 nanotube array as OER electro-catalyst for water electrolysis. *International Journal of Hydrogen Energy* **2017,** *42* (6), 3572-3578.
41. Valdés, Á.; Qu, Z. W.; Kroes, G. J.; Rossmeisl, J.; Nørskov, J. K., Oxidation and Photo-Oxidation of Water on TiO2 Surface. *The Journal of Physical Chemistry C* **2008,** *112* (26), 9872-9879.
42. Liao, P.; Keith, J. A.; Carter, E. A., Water Oxidation on Pure and Doped Hematite (0001) Surfaces: Prediction of Co and Ni as Effective Dopants for Electrocatalysis. *Journal of the American Chemical Society* **2012,** *134* (32), 13296-13309.
43. Tymińska, N.; Wu, G.; Dupuis, M., Water Oxidation on Oxygen-Deficient Barium Titanate: A First-Principles Study. *The Journal of Physical Chemistry C* **2017,** *121* (15), 8378-8389.
44. Dahan, M. H.; Caspary Toroker, M., Water Oxidation Catalysis with Fe2O3 Constrained at the Nanoscale. *The Journal of Physical Chemistry C* **2017,** *121* (11), 6120-6125.
45. Rossmeisl, J.; Qu, Z. W.; Zhu, H.; Kroes, G. J.; Nørskov, J. K., Electrolysis of water on oxide surfaces. *Journal of Electroanalytical Chemistry* **2007,** *607* (1), 83-89.
46. Zhang, Y.-C.; Li, Z.; Zhang, L.; Pan, L.; Zhang, X.; Wang, L.; Fazal e, A.; Zou, J.-J., Role of oxygen vacancies in photocatalytic water oxidation on ceria oxide: Experiment and DFT studies. *Applied Catalysis B: Environmental* **2018,** *224*, 101-108.
47. Ulman, K.; Nguyen, M.-T.; Seriani, N.; Piccinin, S.; Gebauer, R., A Unified Picture of Water Oxidation on Bare and Gallium Oxide-Covered Hematite from Density Functional Theory. *ACS Catalysis* **2017,** *7* (3), 1793-1804.
48. Majrik, K.; Pászti, Z.; Korecz, L.; Trif, L.; Domján, A.; Bonura, G.; Cannilla, C.; Frusteri, F.; Tompos, A.; Tálas, E., Study of PtOx/TiO2 Photocatalysts in the Photocatalytic Reforming of Glycerol: The Role of Co-Catalyst Formation. *Materials* **2018,** *11* (1927).
49. Munnik, P.; de Jongh, P. E.; de Jong, K. P., Recent Developments in the Synthesis of Supported Catalysts. *Chemical Reviews* **2015,** *115* (14), 6687-6718.
50. Lamai, W.; Bunphung, A.; Junumpun, I.; Wongkaew, A., Synthesis and Characterization of Ni@Pt core-shell catalyst over TiO2 support prepared by incipient wetness impregnation and electroless deposition. *Materials Today: Proceedings* **2019,** *17*, 1396-1402.
51. Tálas, E.; Pászti, Z.; Korecz, L.; Domján, A.; Németh, P.; Szíjjártó, G. P.; Mihály, J.; Tompos, A., PtOx-SnOx-TiO2 catalyst system for methanol photocatalytic reforming: Influence of cocatalysts on the hydrogen production. *Catalysis Today* **2018,** *306*, 71-80.
52. Ahmad, W.; Mehmood, U.; Al-Ahmed, A.; Al-Sulaiman, F. A.; Aslam, M. Z.; Kamal, M. S.; Shawabkeh, R. A., Synthesis of zinc oxide/titanium dioxide (ZnO/TiO2) nanocomposites by wet incipient wetness impregnation method and preparation of ZnO/TiO2 paste using poly(vinylpyrrolidone) for efficient dye-sensitized solar cells. *Electrochimica Acta* **2016,** *222*, 473-480.
53. Yang, H.; Li, X.; Wang, A.; Wang, Y.; Chen, Y., Photocatalytic degradation of methylene blue by MoO3 modified TiO2 under visible light. *Chinese Journal of Catalysis* **2014,** *35* (1), 140-147.

54. Castro, Y.; Durán, A., Ca doping of mesoporous TiO2 films for enhanced photocatalytic efficiency under solar irradiation. *Journal of Sol-Gel Science and Technology* **2016,** *78* (3), 482-491.
55. Lv, C.; Lan, X.; Wang, L.; Yu, Q.; Zhang, M.; Sun, H.; Shi, J., Alkaline-earth-metal-doped TiO2 for enhanced photodegradation and H2 evolution: insights into the mechanisms. *Catalysis Science & Technology* **2019,** *9* (21), 6124-6135.
56. Colón, G., Hidalgo, M.C., Navío, J.A., Kubacka, A., Fernández-García, M., Influence of sulfur on the structural, surface properties and photocatalytic activity of sulfated TiO2. *Appl. Catal. B: Environ.* **2009,** *90* (3-4), 633-641.
57. Valero, J. M.; Obregón, S.; Colón, G., Active Site Considerations on the Photocatalytic H2 Evolution Performance of Cu-Doped TiO2 Obtained by Different Doping Methods. *ACS Catal.* **2014,** *4* (10), 3320-3329.
58. Kresse, G.; Hafner, J., *Ab initio* molecular-dynamics simulation of the liquid-metal-amorphous-semiconductor transition in germanium. *Physical Review B* **1994,** *49* (20), 14251-14269.
59. Furthmüller, J.; Hafner, J.; Kresse, G., Dimer reconstruction and electronic surface states on clean and hydrogenated diamond (100) surfaces. *Physical Review B* **1996,** *53* (11), 7334-7351.
60. Blöchl, P. E., Projector augmented-wave method. *Physical Review B* **1994,** *50* (24), 17953-17979.
61. Kresse, G.; Joubert, D., From ultrasoft pseudopotentials to the projector augmented-wave method. *Physical Review B* **1999,** *59* (3), 1758-1775.
62. Perdew, J. P.; Burke, K.; Ernzerhof, M., Generalized gradient approximation made simple. *Physical Review Letters* **1996,** *77* (18), 3865-3868.
63. Morgan, B. J.; Watson, G. W., A DFT + U description of oxygen vacancies at the TiO2 rutile (1 1 0) surface. *Surface Science* **2007,** *601* (21), 5034-5041.
64. Nolan, M.; Elliott, S. D.; Mulley, J. S.; Bennett, R. A.; Basham, M.; Mulheran, P., Electronic structure of point defects in controlled self-doping of the TiO2 (110) surface: Combined photoemission spectroscopy and density functional theory study. *Physical Review B* **2008,** *77* (23), 235424.
65. Iwaszuk, A.; Nolan, M., Reactivity of sub 1 nm supported clusters: (TiO2)n clusters supported on rutile TiO2 (110). *Physical Chemistry Chemical Physics* **2011,** *13* (11), 4963-4973.
66. Nolan, M., Electronic coupling in iron oxide-modified TiO2 leads to a reduced band gap and charge separation for visible light active photocatalysis. *Physical Chemistry Chemical Physics* **2011,** *13* (40), 18194-18199.
67. Fronzi, M.; Iwaszuk, A.; Lucid, A.; Nolan, M., Metal oxide nanocluster-modified TiO 2 as solar activated photocatalyst materials. *Journal of Physics: Condensed Matter* **2016,** *28* (7), 074006.
68. Fronzi, M.; Nolan, M., Surface Modification of Perfect and Hydroxylated TiO2 Rutile (110) and Anatase (101) with Chromium Oxide Nanoclusters. *ACS Omega* **2017,** *2* (10), 6795-6808.
69. Anisimov, V. I.; Zaanen, J.; Andersen, O. K., Band theory and Mott insulators: Hubbard U instead of Stoner I. *Physical Review B* **1991,** *44* (3), 943-954.
70. Dudarev, S. L.; Botton, G. A.; Savrasov, S. Y.; Humphreys, C. J.; Sutton, A. P., Electron-energy-loss spectra and the structural stability of nickel oxide: An LSDA+U study. *Physical Review B* **1998,** *57* (3), 1505-1509.
71. Subbaraman, R.; Tripkovic, D.; Strmcnik, D.; Chang, K.-C.; Uchimura, M.; Paulikas, A. P.; Stamenkovic, V.; Markovic, N. M., Enhancing Hydrogen Evolution Activity in Water Splitting by Tailoring Li⁺-Ni(OH)₂-Pt Interfaces. *Science* **2011,** *334* (6060), 1256-1260.
72. Zhijiao Wu, S. C., Kai Guo, Lingyu Piao. , Effect of aspect ratios of rutile TiO2 nanorods on overall photocatalytic water splitting performance. *Nanoscale,* **2020,** *12*, 4895-4902.
73. Yukari Yamazaki, K. A., Ryuzi Katoh, Suzuko Yamazaki. , Developing Active TiO2 Nanorods by Examining the Influence of Morphological Changes from Nanorods to Nanoparticles on Photocatalytic Activity. *ACS Appl. Nano Mater.* **2018,** *1* (10), 5927-5935.
74. Colón, G. H., M. C.; Munuera, G.; Ferino, I.; Cutrufello, M. G.; Navío, J. A., Structural and surface approach to the enhanced photocatalytic activity of sulfated TiO2 photocatalyst. *Appl. Catal. B: Environ.* **2006,** *63* (1),

45-59.
75. Christoforidis, K. C.; Fornasiero, P., Photocatalytic Hydrogen Production: A Rift into the Future Energy Supply. *ChemCatChem* **2017,** *9* (9), 1523-1544.
76. Xiang, Z.; Zhong, J.; Huang, S.; Li, J.; Chen, J.; Wang, T.; Li, M.; Wang, P., Efficient charge separation of Ag2CO3/ZnO composites prepared by a facile precipitation approach and its dependence on loading content of Ag2CO3. *Materials Science in Semiconductor Processing* **2016,** *52*, 62-67.
77. Haja Hameed, A. S.; Karthikeyan, C.; Sasikumar, S.; Senthil Kumar, V.; Kumaresan, S.; Ravi, G., Impact of alkaline metal ions Mg2+, Ca2+, Sr2+ and Ba2+ on the structural, optical, thermal and antibacterial properties of ZnO nanoparticles prepared by the co-precipitation method. *Journal of Materials Chemistry B* **2013,** *1* (43), 5950-5962.
78. Zaki, M. I.; Ramadan, W.; Katrib, A.; Rabee, A. I. M., Surface chemical and photocatalytic consequences of Ca-doping of BiFeO3 as probed by XPS and H2O2 decomposition studies. *Applied Surface Science* **2014,** *317*, 929-934.
79. Olowoyo, J. O.; Kumar, M.; Singhal, N.; Jain, S. L.; Babalola, J. O.; Vorontsov, A. V.; Kumar, U., Engineering and modeling the effect of Mg doping in TiO2 for enhanced photocatalytic reduction of CO2 to fuels. *Catalysis Science & Technology* **2018,** *8* (14), 3686-3694.
80. Song, Z.; Fan, J.; Xu, H., Strain-induced water dissociation on supported ultrathin oxide films. *Scientific Reports* **2016,** *6*, 22853.
81. Jung, J.; Shin, H.-J.; Kim, Y.; Kawai, M., Controlling water dissociation on an ultrathin MgO film by tuning film thickness. *Physical Review B* **2010,** *82* (8), 085413.
82. Mu, R.; Zhao, Z.-j.; Dohnálek, Z.; Gong, J., Structural motifs of water on metal oxide surfaces. *Chemical Society Reviews* **2017,** *46* (7), 1785-1806.
83. Hu, X. L.; Carrasco, J.; Klimeš, J.; Michaelides, A., Trends in water monomer adsorption and dissociation on flat insulating surfaces. *Physical Chemistry Chemical Physics* **2011,** *13* (27), 12447-12453.
84. Fujimori, Y.; Zhao, X.; Shao, X.; Levchenko, S. V.; Nilius, N.; Sterrer, M.; Freund, H.-J., Interaction of Water with the CaO(001) Surface. *The Journal of Physical Chemistry C* **2016,** *120* (10), 5565-5576.
85. Haertelt, M.; Fielicke, A.; Meijer, G.; Kwapien, K.; Sierka, M.; Sauer, J., Structure determination of neutral MgO clusters—hexagonal nanotubes and cages. *Physical Chemistry Chemical Physics* **2012,** *14* (8), 2849-2856.
86. Byrne, C.; Rhatigan, S.; Hermosilla, D.; Merayo, N.; Blanco, Á.; Michel, M. C.; Hinder, S.; Nolan, M.; Pillai, S. C., Modification of TiO2 with hBN: high temperature anatase phase stabilisation and photocatalytic degradation of 1,4-dioxane. *Journal of Physics: Materials* **2019,** *3* (1), 015009.
87. Malliavin, M. J.; Coudray, C., Ab initio calculations on (MgO)n, (CaO)n, and (NaCl)n clusters (n=1–6). *The Journal of Chemical Physics* **1997,** *106* (6), 2323-2330.
88. Yan, J.; Hummelshøj, J. S.; Nørskov, J. K., Formation energies of group I and II metal oxides using random phase approximation. *Physical Review B* **2013,** *87* (7), 075207.
89. Chen, M.; Felmy, A. R.; Dixon, D. A., Structures and Stabilities of (MgO)n Nanoclusters. *The Journal of Physical Chemistry A* **2014,** *118* (17), 3136-3146.
90. Chen, M.; Thanthiriwatte, K. S.; Dixon, D. A., Structures and Stabilities of (CaO)n Nanoclusters. *The Journal of Physical Chemistry C* **2017,** *121* (41), 23025-23038.
91. Chrétien, S.; Metiu, H., Electronic Structure of Partially Reduced Rutile TiO2(110) Surface: Where Are the Unpaired Electrons Located? *The Journal of Physical Chemistry C* **2011,** *115* (11), 4696-4705.
92. Deskins, N. A.; Rousseau, R.; Dupuis, M., Distribution of Ti3+ Surface Sites in Reduced TiO2. *The Journal of Physical Chemistry C* **2011,** *115* (15), 7562-7572.
93. Miyoshi, A.; Nishioka, S.; Maeda, K., Water Splitting on Rutile TiO2-Based Photocatalysts. *Chemistry – A European Journal* **2018,** *24* (69), 18204-18219.

94. Zhang, X.; Klaver, P.; van Santen, R.; van de Sanden, M. C. M.; Bieberle-Hütter, A., Oxygen Evolution at Hematite Surfaces: The Impact of Structure and Oxygen Vacancies on Lowering the Overpotential. *The Journal of Physical Chemistry C* **2016,** *120* (32), 18201-18208.
95. Nguyen, M.-T.; Piccinin, S.; Seriani, N.; Gebauer, R., Photo-Oxidation of Water on Defective Hematite(0001). *ACS Catalysis* **2015,** *5* (2), 715-721.